J. Fluid Mech. (2008), *vol.* 602, *pp.* 129–174.
doi:10.1017/S002211200800075X Printed in the United Kingdom

Linked twist map formalism in two and three dimensions applied to mixing in tumbled granular flows

R. STURMAN[1], S. W. MEIER[2], J. M. OTTINO[2,3] AND S. WIGGINS[4]

[1]Department of Applied Mathematics, University of Leeds, Leeds LS2 9JT, UK
r.sturman@maths.leeds.ac.uk

[2]Department of Chemical and Biological Engineering, Northwestern University, Evanston, IL 60208, USA
smeier@chem-eng.northwestern.edu

[3]The Northwestern Institute on Complex Systems (NICO), Northwestern University, Evanston, IL 60208, USA
jm-ottino@northwestern.edu

[4]School of Mathematics, University of Bristol, Bristol BS8 1TW, UK
s.wiggins@bristol.ac.uk

(Received 1 September 2007 and in revised form 21 January 2008)

We study the mixing properties of two systems: (i) a half-filled quasi-two-dimensional circular drum whose rotation rate is switched between two values and which can be analysed in terms of the existing mathematical formalism of linked twist maps; and (ii) a half-filled three-dimensional spherical tumbler rotated about two orthogonal axes bisecting the equator and with a rotational protocol switching between two rates on each axis, a system which we call a three-dimensional linked twist map, and for which there is no existing mathematical formalism. The mathematics of the three-dimensional case is considerably more involved. Moreover, as opposed to the two-dimensional case where the mathematical foundations are firm, most of the necessary mathematical results for the case of three-dimensional linked twist maps remain to be developed though some analytical results, some expressible as theorems, are possible and are presented in this work. Companion experiments in two-dimensional and three-dimensional systems are presented to demonstrate the validity of the flow used to construct the maps. In the quasi-two-dimensional circular drum, bidisperse (size-varying or density-varying) mixtures segregate to form lobes of small or dense particles that coincide with the locations of islands in computational Poincaré sections generated from the flow model. In the 3d spherical tumbler, patterns formed by tracer particles reveal the dynamics predicted by the flow model.

1. Introduction

While the study of mixing of fluids has received a great deal of attention recently, there has been comparatively little research into the mixing of granular materials. This is in spite of the ubiquity and range of situations in industrial, experimental and natural processes. For example, an understanding of the behaviour of granular materials is a crucial step in many pharmaceutical, food, chemical, ceramic, metallurgical and construction industries. One reason for the difference in levels of understanding

is that while miscible fluids mix via molecular diffusion, granular materials often have a tendency to segregate based on particle properties such as size and density. Nevertheless, it is appropriate to apply many of the same tools to both problems, in particular, ideas from dynamical systems theory (Meier, Lueptow & Ottino 2007).

The study of mixing of fluids significantly benefited from the adoption of tools from nonlinear dynamics and its connection with chaos. A few flows played an essential role. Thus, for example, the blinking vortex flow (Aref 1984), though idealized, served as a springboard for many of the studies that followed. The rotating quasi-two-dimensional granular tumbler with circular cross-section may play a similar role in granular mixing. Flow in the quasi-two-dimensional circular tumbler is restricted to two dimensions because the axial dimension of the tumbler is much smaller than the radial dimension of the tumbler. Thus, the magnitude of the axial flow is negligible compared to the magnitude of the streamwise flow. In experiments, the two-dimensional dynamics of the flow can be observed through a clear endwall.

Fiedor & Ottino (2005) studied granular mixing and segregation in a half-filled quasi-two-dimensional circular tumbler rotated in a time-dependent manner generating time-periodicity in the granular flow. Here, we propose a granular tumbler flow analogous to the blinking vortex fluid flow with a rotation rate that alternates between two different values in a stepwise manner. One may think that this quasi-two-dimensional flow is the simplest system for studying granular mixing that has a clean mathematical representation. There is, however, a second system that, while on first viewing may appear to be physically more complicated, is in fact simpler since it does not require physical fine tuning such as controlling the thickness of the device to achieve the quasi-two-dimensional approximation needed to match the experiment to the mathematical model. This is a three-dimensional system, a half-filled spherical tumbler rotated by two orthogonal axes bisecting the equator of the sphere and operated with a rotational protocol that switches between rotation around each axis at constant angular rotation rates. We call this system a three-dimensional linked twist map. The system can be modelled based on the experimental results of Pohlman *et al.* (2006*a*), and requires no experimental fine-tuning, such as elimination of endwall effects. As we shall see, the mathematics becomes considerably more involved, the possible computational outcomes considerably richer, and the experimental results significantly more involved given the difficulties in imaging the interior of opaque media. Moreover, as opposed to the two-dimensional case, where the mathematical foundations are firm, most of the necessary mathematics for the case of three-dimensional linked twist maps remains to be developed.

Linked twist maps embody the notion of 'streamline crossing', which is known to be a mechanism for enhancing mixing (Ottino 1989; Sturman, Ottino & Wiggins 2006). The linked twist map formalism gives considerable analytical insight into a field that has typically resorted to numerical computations and where analytical predictions are rare. In particular, it provides the formalism for proving the existence of the mathematically strongest possible mixing property (the Bernoulli property) on a set of positive area in the domain of the flow. Using the formalism of linked twist maps in the two-dimensional case, in this paper we are able to develop a strategy for understanding the structure and formation of islands. This is significant since islands can be directly correlated with patterns of segregation.

Experiments in fluids using two-dimensional flow involve injecting blobs of dyed fluid in strategic locations and directly observing the deformation and folding of dye patterns, or resorting to two-dimensional cuts with laser sheets in three-dimensional systems (Fountain, Khakhar & Ottino 1998). Such experiments are more complicated

and often impossible in granular flows unless coarse resolutions are acceptable. Surprisingly, one class of experiments involving granular matter is easier to set up. These are segregation experiments, a case where the physics is undoubtedly more complicated as these involve two classes of particles varying in either particle size or density – leading to unmixed patterns that offer evidence of the soundness of the underlying flow description (figure 1).

Results in two and three dimensions are presented here as an indication of the possibilities and coarse qualitative agreement, and to show general matching between analytical and computational results and underlying symmetries of the flow as displayed by the experiments, rather than a direct quantitative prediction of specific experiments by theory. We show also the results of segregation as predicted by a computational simulation, though no presentation of the numerical model, except for a reference, is given about the details of the model itself.

2. Rotating tumbler mixers in two dimensions

2.1. *Circular tumblers with constant angular velocity*

Consider a rotating quasi-two-dimensional circular tumbler of radius L half-filled with a granular material. Note that for the two-dimensional circular tumbler which we discuss in § 2 we could non-dimensionalize out the radius L, and set it to unity. We retain L as a parameter here as we will require it for our discussion of three-dimensional spherical mixers in § 3. Granular flows in rotating tumblers can be categorized into several different flow regimes. The Froude number, $Fr = \omega^2 L/g$ (where L is the tumbler radius, ω is the rotation rate of the tumbler, and g is acceleration due to gravity), provides a ratio of the inertial force to the gravitational force to identify the different flow regimes of dry granular material (Henein, Brimacombe & Watkinson 1983; Mellmann 2001; Brucks *et al.* 2007). When the Froude number is very small ($Fr < 10^{-5}$) , the granular material flows in intermittent avalanches at the free surface. When $Fr \geqslant 1$, the granular material rotates in solid-body rotation with the tumbler walls. For the intermediate range $10^{-4} < Fr < 10^{-2}$ that is the subject of this paper, the flow in the tumbler is in what is referred to as the rolling or continuous-flow regime (Henein *et al.* 1983; Mellmann 2001; Brucks *et al.* 2007; Rajchenbach 1990). It is characterized by a thin, rapidly flowing, flat surface layer that flows at an angle, the dynamic angle of repose, with respect to the horizontal (Rajchenbach 1990; Duran 2000; Ristow 2000). In our experiments, the flowing layer is approximately 5–10 particles thick (Jain *et al.* 2002). Particles enter this flowing layer on the upstream end from a fixed bed (the *bulk*) in solid-body rotation with the tumbler. Particles exit the flowing layer on the downstream end and return to the bed of solid-body rotation.

A continuum model of the behaviour of the continuous-flow regime in a quasi-two-dimensional tumbler is given in Fiedor & Ottino (2005) based on work by Khakhar *et al.* (1997, 1999, 2001) and Makse (1999). This model is the basis for the mixing studies in this paper. There is a substantial amount of experimental evidence that these models capture the segregation patterns observed in experiments using polydisperse granular materials varying in either size or density. Though this is not direct confirmation of the velocity field itself, the weight of evidence is compelling and the agreement between Poincaré sections using the velocity field and experiments is clear (as shown in figure 1). Moreover the results are robust: they are largely independent of the materials used and hold for dry granular systems, referred to as DGS (granular materials wholly immersed in air), as well as for liquid granular

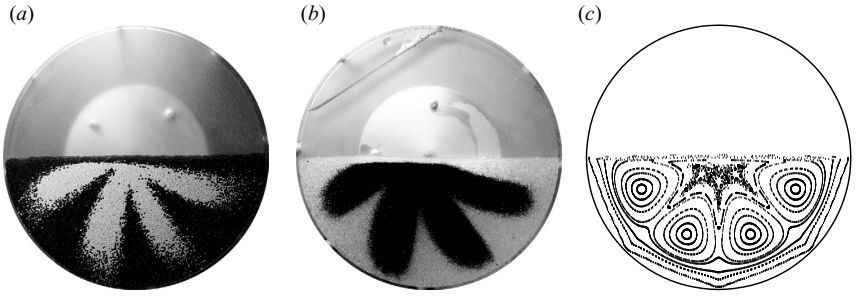

FIGURE 1. This figure illustrating the agreement between experimental and numerical systems, both liquid and dry, is taken from Sturman *et al.* (2006). A larger number of figures supporting this agreement can be found in, for example, Fiedor & Ottino (2005). (*a*) DGS, (*b*) LGS, (*c*) Poincaré section.

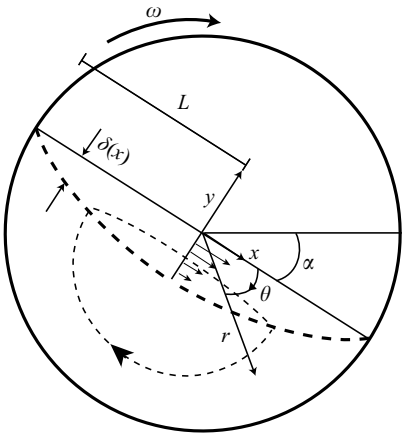

FIGURE 2. The geometry of a circular tumbler rotating at a constant angular velocity, showing the interface between the bulk and the flowing layer as a solid dotted line, and a closed streamline passing through both the bulk and the flowing layer as a dotted line. The thickness of the layer has been exaggerated.

systems, LGS (where the granular matter is wholly immersed in a liquid). Figure 1 shows representative examples.

The motion of a particle in this model (approximated by a point tracer in a fluid mechanical sense) consists of two parts. Particles in the bulk undergo solid-body rotation and move along circular arcs in solid-body rotation with the tumbler. If the tumbler rotates with an angular velocity ω, the velocity components of the particles in the bulk are given by

$$v_r = 0, \tag{2.1}$$

$$v_\theta = r\omega, \tag{2.2}$$

in polar coordinates centred at the centre of the tumbler. The coordinate axes x and y of the flow in the flowing layer are fixed in space, but are rotated through the dynamic angle of repose, denoted by α. The polar coordinates r, θ are defined with respect to the x, y coordinate system, but they are oriented differently to the standard system: θ increases in the clockwise sense (the sense of rotation of the cylinder) rather than the usual counterclockwise convention (see figure 2). This implies

that

$$x = r\cos\theta,$$
$$y = -r\sin\theta.$$

Particles leave the bulk when they enter the flowing layer. The shape of the flowing layer is given by the parabola

$$\delta = \delta(x) = \delta_0\sqrt{1 - \frac{x^2}{L^2}}, \tag{2.3}$$

where $\delta_0 = \delta_0(\omega)$ is the maximum thickness of the flowing layer. (The square root in equation (2.3) appears in some models but not others (Khakhar *et al.* 1997; Hill *et al.* 1999). It is important to stress that largely identical results occur with a model of the form $\delta(x) = \delta_0(1 - x^2/L^2)$.) It is assumed that the surface of the granulate is always horizontal.

Particles in the flowing layer move according to a continuous downhill flow. We assume the velocity in the flowing layer varies linearly with depth and that the shear rate $\dot{\gamma}$ is constant. As derived in Fiedor & Ottino (2005), we therefore have streamwise and transverse components of the velocity given by

$$v_x = \dot{\gamma}(\delta(x) + y), \tag{2.4}$$
$$v_y = \frac{\omega x y}{\delta(x)}, \tag{2.5}$$

in Cartesian coordinates also centred at the centre of the tumbler. Mass conservation of the granular system means that the constant shear rate $\dot{\gamma}$ takes the value $\dot{\gamma} = \omega L^2/\delta_0^2$.

We define precisely the domains D_{b,δ_0} (the bulk) and D_{f,δ_0} (the flowing layer) as follows:

$$D_{f,\delta_0} = \{(x, y) \,|\, -L \leqslant x \leqslant L,\ 0 \leqslant y < -\delta(x)\}, \tag{2.6}$$
$$D_{b,\delta_0} = \{(r, \theta) \,|\, 0 \leqslant r \leqslant L,\ 0 \leqslant \theta < \pi\} - D_{f,\delta_0}. \tag{2.7}$$

Note that the relative sizes of the domains depend on δ_0, the depth of the flowing layer. The relative time spent in each domain can be approximated as follows. Consider a particle in the flowing layer. The depthwise average streamwise velocity in the layer is $\bar{v}_x = \dot{\gamma}\delta(x)/2$. Integrating over the length of the flowing layer yields the time it takes a particle to cross the flowing layer, while the time spent circumnavigating the bulk approaches π/ω for a thin flowing layer ($\delta_0 \ll L$). Thus

$$\frac{\text{Time in flowing layer}}{\text{Time in bulk}} \propto \sqrt{\frac{\omega}{\dot{\gamma}}}.$$

A limiting case corresponds to the situation where the flow in the layer is very fast compared with the flow in the bed. This can be thought of as the thickness of the layer $\delta_0 \to 0$. This limiting case clearly is of little value in the case of two-dimensional blinking flows as the elimination of the layer itself results in no mixing. The limiting case, however, can be used to examine aspects of three-dimensional blinking flows, a case we examine in § 3.6.1.

For ω constant, particle streamlines form closed loops passing through the flowing layer. Moreover, this system of differential equations describing the motion of particles is steady, divergence free, and integrable. We will exploit the consequences of this

more fully in the next section. The geometry of this system, together with the general aspect of streamlines, is illustrated in figure 2.

2.1.1. *Characterizing particle kinematics by a twist map: action–angle variables for the circular tumbler rotating with constant velocity*

The 'mapping approach' to study fluid particle kinematics is well-established (see, e.g. Ottino 1989; Sturman *et al.* 2006). In this approach, the motion of fluid particles is reduced to a discrete time map, which in this context is typically referred to as a *Poincaré map*. In practice, this means that rather than observe a fluid particle tracing out a continuous curve in the domain, we instead 'stroboscopically' view the particle at fixed discrete intervals of time. The collection of discrete points in the flow domain obtained in this way is referred to as a *Poincaré section*. Poincaré sections can give a good picture of the mixing properties of a given flow.

For the circular tumbler rotating at constant angular velocity, the flow is steady and the streamlines form closed concentric loops. The velocity field defined by (2.1), (2.2), (2.4) and (2.5) is two-dimensional, steady, and area preserving. Such velocity fields can be expressed as a Hamiltonian system, with the streamfunction playing the role of the Hamiltonian function (see e.g. Ottino 1989; Samelson & Wiggins 2006). The streamfunction for the flow in the bulk, expressed in Cartesian coordinates, is given by

$$\psi_b(x, y) = \tfrac{1}{2}\omega(x^2 + y^2),$$

and the streamfunction for the flow in the flowing layer is given by

$$\psi_f(x, y) = \dot{\gamma}\, y\big(\delta + \tfrac{1}{2}y\big). \tag{2.8}$$

In regions of closed streamlines of Hamiltonian systems, a convenient set of coordinates can be found, called *action–angle coordinates* (Wiggins 2003; Samelson & Wiggins 2006), that can be viewed as a nonlinear generalization of standard polar coordinates in the sense that one coordinate, ρ, labels the streamline and is constant in time (essentially it is the area enclosed by the streamline) and the other coordinate, ϕ, is an angular coordinate that evolves linearly in time (but the rate of change, or frequency, depends on ρ). Action–angle variables play an important role in characterizing the particle kinematics in terms of a *twist map*. Therefore we will discuss first the definition of action–angle variables for this flow, and then show how they are used to define a twist map.

The construction of action–angle variables in regions of closed streamlines is standard in the case where the streamlines are defined by a single streamfunction. The situation is slightly more complicated in our case since the flow consists of two distinct regions with different streamfunctions in each region. Consequently, we must take additional care in developing the setting where the construction of action–angle variables can be carried out.

We begin by describing the flow domain in a more quantitative manner. Having defined D_{f,δ_0} and D_{b,δ_0} in (2.6) and (2.7), the boundary between D_{f,δ_0} and D_{b,δ_0}, denoted $\partial_{f,b}$, is therefore given by

$$\partial_{f,b} = \{(x, y)\,|\, -L \leqslant x \leqslant L,\ y = -\delta(x)\}.$$

The domain of the flow is given by $D_{f,\delta_0} \cup D_{b,\delta_0}$. We define the flow on each region separately, with a matching condition for the streamlines at the boundary. Let

$$\psi(x, y) = \begin{cases} \psi_f(x, y) & \text{on} \quad D_{f,\delta_0}, \\ \psi_b(x, y) & \text{on} \quad D_{b,\delta_0}. \end{cases} \tag{2.9}$$

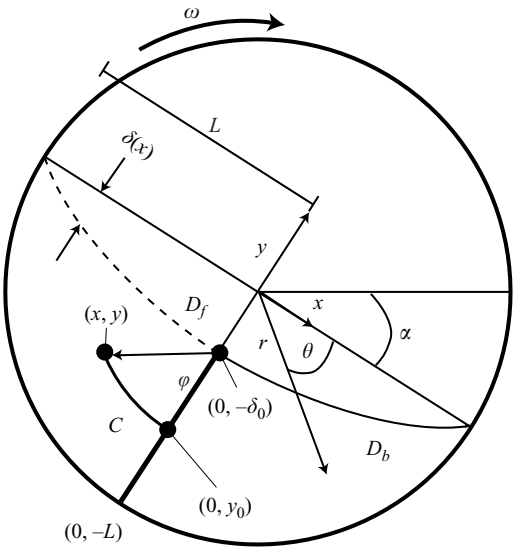

FIGURE 3. The geometry associated with the construction of action–angle variables for the circular tumbler mixer rotating at a constant angular velocity.

If a particle crosses $\partial_{f,b}$ with $x > 0$, then it is leaving D_{f,δ_0} and entering D_{b,δ_0}. If it is crossing $\partial_{f,b}$ with $x < 0$, then it is leaving D_{b,δ_0} and entering D_{f,δ_0}.

Formally, (2.9) defines a streamfunction for the entire domain. However, *a priori*, it does not have the usual property that the level sets of $\psi(x, y)$, i.e. $\psi(x, y) = \psi = \text{constant}$, are closed trajectories. This is because the union of $\psi_f(x, y) = \psi = \text{constant}$ and $\psi_b(x, y) = \psi = \text{constant}$ may not define a closed streamline in all of the domain, i.e. the two level sets in D_{f,δ_0} and D_{b,δ_0} may not meet at the boundary, $\partial_{f,b}$. This situation is easily addressed by noting that adding an arbitrary constant to a streamfunction does not change the corresponding velocity field. Consider a trajectory that passes from the flowing layer to the bulk at $(x_1, y_1) = (x_1, -\delta(x_1))$, and let $\psi_f(x_1, -\delta(x_1)) = \psi_f$ and $\psi_b(x_1, -\delta(x_1)) = \psi_b$. Then we redefine $\psi_f(x, y)$ as $\tilde{\psi}_f(x, y) = \psi_f(x, y) + \psi_b - \psi_f$ for which we now have $\tilde{\psi}_f(x_1, -\delta(x_1)) = \psi_f(x_1, -\delta(x_1)) + \psi_b - \psi_f = \psi_b$. We then replace $\psi_f(x, y)$ by $\tilde{\psi}_f(x, y)$ and we have the desired property.

Now we are in a position to give the definition of the transformation to the action–angle coordinates, and describe their relationship to the geometry of closed streamlines. Let C denote a reference line between the points $(0, -\delta_0)$ and $(0, -L)$ (figure 3). The line C plays the role of a set of initial conditions, and could be any arbitrary curve intersecting each closed trajectory. We represent C in parametric form as follows:

$$C = \{(0, y_0)) \in \mathbb{R}^2 \mid -\delta_0 \geqslant y_0 \geqslant -L\},$$

and trajectories starting on C are represented by $(x(t), y(t))$ where $x(0) = 0$ and $y(0) = y_0$. Let (x, y) be an arbitrary point on a closed streamline traced out by the trajectory $(x(t), y(t))$ and let $t = t(x, y)$ be the time taken for the trajectory starting at $(0, y_0)$ to flow to the point (x, y). We denote the period of each closed trajectory defined by $\psi(x, y) = \psi = \text{ constant}$ by $T(\psi)$. The *angle variable*, $\phi(x, y)$, is now defined as:

$$\phi(x, y) = \frac{2\pi}{T(\psi)} t(x, y), \tag{2.10}$$

where $(x, y) \in \psi = \text{constant}$ (figure 3).

The area enclosed by any closed streamline is clearly constant in time. We use this to define the *action variable*, denoted $\rho(x, y)$, as

$$\rho = \frac{1}{2\pi} \oint_{\psi} x \, \mathrm{d}y, \tag{2.11}$$

where ψ labels the closed streamline defined by $\psi(x, y) = \psi = \text{constant}$. It should be clear from (2.11) that the action variable for a closed streamline is a function of ψ, which we explicitly denote as:

$$\rho = \rho(\psi),$$

and that this relationship can be inverted as a result of the one-to-one relationship between closed streamlines and the area they enclose:

$$\psi = \psi(\rho).$$

We can also label the period of each closed streamline by either ρ or ψ.

We have thus defined coordinates (ρ, ϕ) on a region of closed streamlines such that the velocity field is given by

$$\begin{aligned} \dot{\rho} &= 0, \\ \dot{\phi} &= \frac{2\pi}{T(\rho)} \equiv \Omega(\rho), \end{aligned} \tag{2.12}$$

where $\Omega(\rho)$ is the frequency associated with the closed streamline having action ρ. The trajectories of (2.12) are easily obtained as

$$\begin{aligned} \rho(t) &= \rho_0 = \text{constant}, \\ \phi(t) &= \frac{2\pi}{T(\rho)} t + \phi_0 \equiv \Omega(\rho) t + \phi_0. \end{aligned} \tag{2.13}$$

It is shown in Wiggins (2003) that the Jacobian of the transformation to action–angle coordinates is identically one, which implies that area is preserved under the action–angle transformation, and that the 'Hamiltonian structure' is also preserved under action–angle transformations. This latter point means that if we take the streamfunction in the original (x, y) coordinates and transform it to action–angle coordinates (ρ, ϕ), then the velocity field in action–angle coordinates may be obtained from this transformed streamfunction in the usual way. More importantly, the transformed streamfunction is a function of just the ρ variable.

We consider the motion of particles in terms of a map. The map is constructed from the trajectories (2.13) and is obtained by considering the evolution of particles for a fixed interval of time, which we will take to be $t = \tau/2$ (the reason for the factor of a half will be made clear in § 2.2). Therefore, the mapping of points is given by

$$P(\rho, \phi) = \left(\rho, \phi + \Omega(\rho) \frac{\tau}{2} \right). \tag{2.14}$$

This is an example of a *twist map* since $\Omega(\rho)$ is a monotonic function of ρ which is responsible for shearing, or 'twisting' a line of initial conditions transverse to the streamlines.

Periodic points of period n of a map are points having the property that they return to their starting point after n iterations of the map. Periodic points of two-dimensional mappings can be classified into three types: hyperbolic, elliptic or parabolic. These

three terms refer to properties of the eigenvalues of the matrix associated with the linearization of the map at the periodic point (note that since the map preserves area, the product of the eigenvalues is one). Hyperbolic means that the two eigenvalues are real, one with absolute value less than one and the other with absolute value greater than one, elliptic means that the eigenvalues are not real, but each has modulus one, and parabolic means that the eigenvalues are real and have modulus one. The linearized behaviour near hyperbolic periodic points exhibits a strongly (that is, at an exponential rate) contracting and a strongly expanding direction, i.e. they are saddle points. The linearized behaviour near an elliptic periodic point exhibits rotational motion. Under generic conditions elliptic periodic points give rise to regions of unmixed fluids since they are surrounded by closed material curves that are barriers to mixing. These are the so-called 'KAM curves', which create 'islands' of unmixed fluid (see e.g. Ottino 1989; Samelson & Wiggins 2006; Sturman *et al.* 2006). One of the significant characteristics of hyperbolic and elliptic periodic points is that the linearized dynamics is 'qualitatively the same' as the nonlinear dynamics near the periodic point. However, the behaviour near a parabolic periodic point cannot be determined solely from linearized behaviour, the effect of nonlinear terms is crucial. Depending on the nature of the nonlinear terms, parabolic periodic points may be surrounded by closed 'KAM curves' , or they may possess separatrices (see e.g. Simo 1980, 1982; Aharonov & Elias 1990). In either case, they do give rise to islands of unmixed fluid, which is the essential feature that is relevant to us.

Since the Jacobian of the twist map P defined by (2.14) is given by

$$DP = \begin{pmatrix} 1 & \dfrac{\tau}{2}\dfrac{\mathrm{d}\Omega(\rho)}{\mathrm{d}\rho} \\ 0 & 1 \end{pmatrix}, \tag{2.15}$$

it is clear that any periodic point which remains on the same streamline $\rho = \text{constant}$ is parabolic, since DP has a double unit eigenvalue. As described above, all points are constrained to lie on a unique streamline. In the following section, we introduce a time-dependent version of the angular rotation, which allows trajectories to visit different streamlines.

2.2. *Time-dependent angular rotation: the blinking tumbler mixer*

The twist map (2.14) is integrable in the sense that orbits of points under the action of the map lie on closed curves, i.e. the streamlines. If the flow becomes time-dependent, then the flow generally becomes non-integrable. This leads to the possibility of chaotic motion which one would believe would lead to 'good mixing', but it is also possible for regions that do not mix to exist within the regions of chaos ('islands'). In Fiedor & Ottino (2005) the tumbler flow was made unsteady by modulating the rotation rate ω sinusoidally in time. Here, we will follow the same approach, but rather than modulate the rotation rate continuously in time, we will switch the rotation rate discontinuously between two fixed frequencies. This is very similar in spirit to the well-known blinking vortex flow first studied in Aref (1984). Accordingly, we will refer to our flow as the *blinking tumbler flow*. As was the case for the blinking vortex flow, this relatively simple form of time-dependence will enable us to gain a great deal of insight into the mechanism of the kinematics without sacrificing the complexity.

Taking Poincaré sections and studying Poincaré maps instead of continuous time equations as a way of extracting fundamental information about fluid systems is a standard technique. This procedure typically involves sampling the flow at

regular intervals in either time or space. In some recent studies of quasi-two-dimensional granular mixers, polygonal tumblers are used (Khakhar *et al.* 1999; Cisar, Umbanhowar & Ottino 2006). This gives a natural periodicity to the rotation (the Poincaré map samples the flow each time the tumbler reaches its original orientation under rotation). For a cylindrical tumbler, the angular position of the tumbler is irrelevant. Thus, the Poincaré map is sampled at every period of the forcing. For the blinking tumbler, we take as the Poincaré map the time-τ map of the flow, which will correspond to one iteration of the linked twist map.

More precisely, the rotation rate of the tumbler is periodically alternated between two constant angular velocities $\omega_a \neq \omega_b$ as follows:

$$\omega = \begin{cases} \omega_b = \bar{\omega} + \hat{\omega} & \text{for } \mathrm{i}\tau < t < (\mathrm{i}+1/4)\tau, \\ \omega_a = \bar{\omega} - \hat{\omega} & \text{for } (\mathrm{i}+1/4)\tau < t < (\mathrm{i}+3/4)\tau, \\ \omega_b = \bar{\omega} + \hat{\omega} & \text{for } (\mathrm{i}+3/4)\tau < t < (\mathrm{i}+1)\tau, \end{cases} \tag{2.16}$$

where we take $\bar{\omega} = 1$ and $\hat{\omega} = 1/3$. In other words, the tumbler is rotated at a rate of ω_a for time $\tau/2$, then at a rate of ω_b for time $\tau/2$, with this sequence of rotation rates repeated indefinitely. We will refer to the instant in time at which the angular velocity changes as a *switching point*.

In our chosen Poincaré section we include an initial 'phase shift' of $t = \tau/4$. This is a largely arbitrary operation, and simply has the effect of shifting the switching times with respect to the rotation of the cylinder. We take $t = \tau/4$, partly as we believe it clarifies the images of the flow structure in later figures, since the Poincaré sections are symmetric about $x = 0$, and partly to establish a close link to Fiedor & Ottino (2005), who include an identical phase shift in their sinusoidally forced rotations. If we denote by N the number of pairs of alternations between ω_a and ω_b ('modulations') in one rotation of the cylinder, we have

$$2\pi = \left(\omega_b \frac{\tau}{4} + \omega_a \frac{\tau}{2} + \omega_b \frac{\tau}{4}\right) N = \left(\frac{\omega_a + \omega_b}{2}\right) N\tau = \bar{\omega} N \tau = N\tau,$$

and therefore,

$$\tau = \frac{2\pi}{N}.$$

The total amount of time required for the cylinder to make one complete revolution, T, is given by $N\tau = T$ or, using the equation above, $T = 2\pi$.

Since the angular rotation takes one of two constant values, $\delta_0 = \delta_0(\omega)$ also alternates between two constant values, for which we take $\delta_{0a} = 0.05$ and $\delta_{0b} = 0.1$. This gives $\dot{\gamma}_a \equiv \omega_a L^2/\delta_0^2 = 800L^2/3$ and $\dot{\gamma}_b \equiv \omega_b L^2/\delta_0^2 = 400L^2/3$. The streamlines for this situation are shown in figure 4, with streamlines for frequency ω_a shown in black and those for ω_b shown in grey.

Numerically computed Poincaré sections for this system are shown in figure 5, for even N, and figure 6, for odd N. For $N = 2$, 4, 6 and 8, the figures share common features. There are $N/2$ large islands, lying at the same radius for each figure, and equally spaced in the angular direction. These islands have a 'rectangular' shape, in that their sides lie roughly along lines of constant r and θ. Also discernible (particularly for $N = 2$, 4) are smaller islands, again at roughly the same radius, in between the large islands. Numerous other small islands may also appear, but the most prominent form this collection of rectangular islands. These islands lie symmetrically

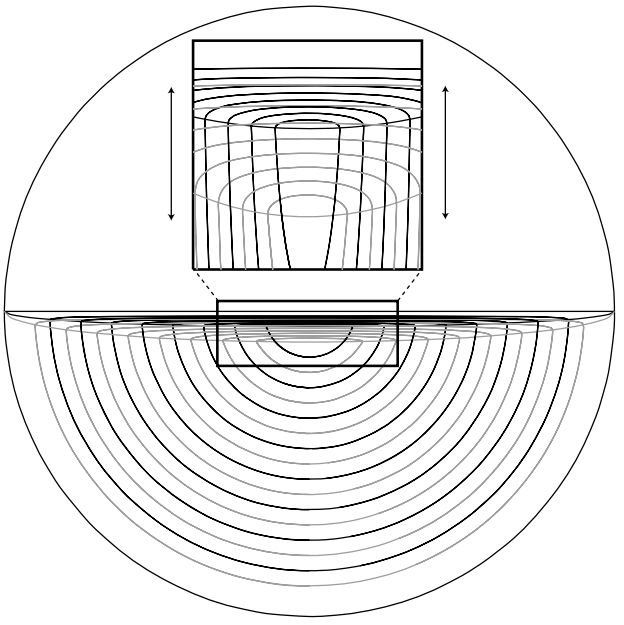

FIGURE 4. Two sets of streamlines of tracers in a rotating tumbler for frequency ω_a shown in black and those for ω_b shown in grey. The two different frequencies give two different depths of the flowing layer, and the overlap (shown in the inset with the vertical direction exaggerated) of the two flowing layers for the two different frequencies is the area of transverse 'streamline crossing'.

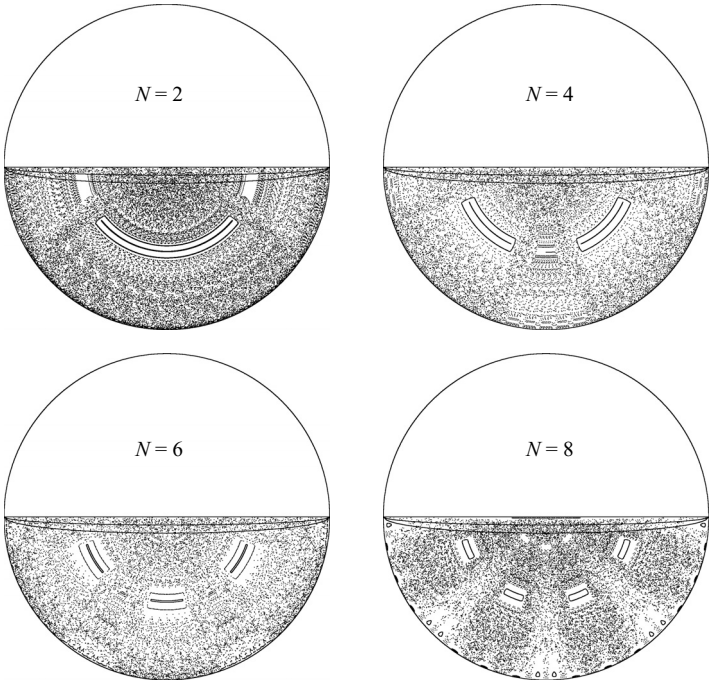

FIGURE 5. Blinking-modulated angular frequency for even modulation, $N = 2, 4, 6, 8$. Parameter values are $\omega_a = 2/3$, $\omega_b = 4/3$, $\delta_{0a} = 0.05$. $\delta_{0b} = 0.1$, $L = 1$, giving $\dot{\gamma}_a = 800/3$, $\dot{\gamma}_b = 400/3$. In each figure the lower boundary of the flowing layer for each frequency is indicated by the parabola.

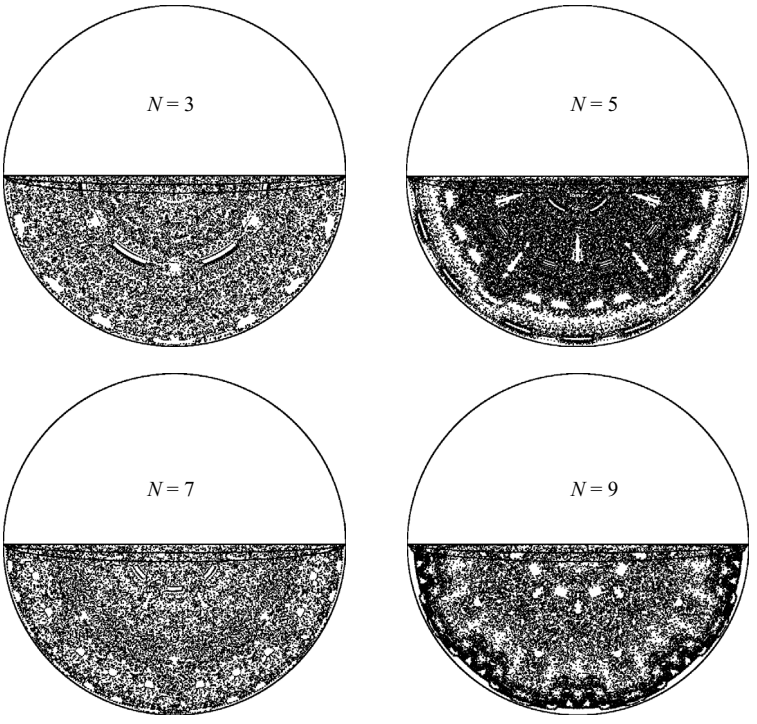

FIGURE 6. Blinking-modulated angular frequency for odd modulation, $N = 3, 5, 7, 9$. Parameter values are as in figure 5.

about the $x = 0$ axis, owing to the choice of phase shift $\tau/4$; a different choice simply leads to the islands appearing at the same radius, but at different angular positions.

Just as was observed in Fiedor & Ottino (2005), there is a dichotomy between the behaviour of the system for even and odd N. Similar rectangular islands appear for $N = 3, 5, 7, 9$, but these are not nearly as prominent as for even N.

2.2.1. *The blinking tumbler mixer as a linked twist map*

Modulating the angular velocity in a blinking fashion has two advantages. First, it allows the system to be cast in the form of a *linked twist map*; secondly, analysis of periodic orbits can be performed and the location and size of the associated islands can be predicted. Linked twist maps form a paradigm for fluid or granular systems which mix by switching their flow patterns periodically in time. They do so by formalizing the ubiquitous concept of 'crossing of streamlines' in a mathematically rigorous way (Sturman *et al.* 2006).

First, we define what we mean by a linked twist map and show how it arises in the setting of the blinking tumbler mixer. Referring to figure 4, the blinking protocol defined by (2.16) means that points evolve for a time $\tau/2$ with frequency ω_a along one streamline pattern (shown in black in figure 4) and then they evolve for a time $\tau/2$ at frequency ω_b along the other streamline pattern (shown in grey in figure 4). Following the discussion in § 2.1.1, the flow in the modulated tumbler can be described as the composition of two maps P_a and P_b. The composition of two twist maps is a *linked twist map*, denoted by $\mathscr{P} \equiv P_b \circ P_a$.

The phenomenon of *streamline crossing* is made explicit in the formulation as a linked twist map. Consider a point $(x_1, y_1) \in D_{b,\delta_{0a}} \cap D_{b,\delta_{0b}}$ (that is, in the intersection of the two bulk regions). Since streamlines for ω_a and ω_b are

coincident in this region (they are circular arcs with the same centre), we have $\psi_a(x_1, y_1) = \psi_b(x_1, y_1) = \psi(\rho) = \text{constant}$, and (x_1, y_1) lies on the same streamline for both ω_a and ω_b. For a point $(x_2, y_2) \in D_{f,\delta_{0a}} \cup D_{f,\delta_{0b}}$ (that is, in either of the two flowing layers), streamlines are not coincident (assuming $\delta_{0a} \neq \delta_{0b}$; see figure 4), and we may have $\psi_a(x_2, y_2) \neq \psi_b(x_2, y_2)$. Thus, any trajectory of $\mathscr{P}$ remaining in $D_{b,\delta_{0a}} \cap D_{b,\delta_{0b}}$ for all time remains on a single streamline and has the dynamics of a single twist map, whereas for streamline crossing, and hence non-trivial, non-integrable, dynamics to occur, a trajectory must enter the union of the flowing layers.

Linked twist maps have been studied in great detail in Burton & Easton (1980), Wojtkowski (1980), Devaney (1978, 1980), Przytycki (1983) and Sturman *et al.* (2006) and they are one of the few types of dynamical systems with a direct relation to applications where it is possible to prove rigorously the existence of ergodicity and the strongest possible mixing properties. However, to achieve the strongest possible mixing properties, the best results have been obtained by assuming rather stringent requirements on either the geometry or the nature of the overlap of the two streamline patterns that define the two twist maps whose composition forms the linked twist map. The currently known requirements for linked twist maps to achieve the best possible mixing are not satisfied for the blinking tumbler mixer. Nevertheless, the mathematical results provide a good guide for studying the mixing properties of the blinking tumbler flow, which we now describe.

Consider the overlap of the two streamline patterns in figure 4. There are three distinct regions that we focus on. One is the bulk, where the streamlines for the two patterns are coincident. Another region is the overlap of the two flowing layers for the two streamline patterns. Here the streamlines for the two patterns are essentially parallel. The final region is the region of the flowing layer that is not in the intersection of the two flowing layers. Here the streamlines for the two patterns are transverse, i.e. they cross.

Roughly, the linked twist map theorems tell us that we want to eliminate (or make as small as possible) regions where the streamlines from the two patterns are parallel, and maximize the size of the regions where the streamlines for the two patterns are transverse (this is the notion of streamline crossing).

Unfortunately for mixing, the blinking tumbler mixer in two dimensions has large regions where the streamline patterns are essentially parallel and only a relatively small region where the two streamline patterns are transverse. Thus, we expect this flow to be a poor mixer unless typical trajectories visit the regions of transverse streamlines sufficiently often. We will see that this expectation of visiting transverse regions is not realized and that mixing is never complete. Nevertheless, these ideas provide a guide for us to predict the size and location of islands, as well as to understand the stability properties of the related periodic orbits.

2.2.2. *Comments and remarks on the study of blinking tumbler mixers as a map*

It is well known that features of the Poincaré map such as chaotic regions and islands organize features of the flow itself. The features which impact most strongly on the flow patterns produced are periodic orbits of low period. As is well-known, hyperbolic periodic orbits tend to be good for chaotic mixing, whereas elliptic periodic orbits tend to be surrounded by islands of unmixed fluid. A third class of periodic orbits form parabolic periodic points which may also give rise to surrounding islands.

Let ξ be a periodic orbit of $\mathscr{P}$. Then the stability of the periodic orbit is governed by the eigenvalues of the matrix formed by multiplying the Jacobians evaluated along

the periodic orbit. Suppose ξ consists of points ξ_i all of which lie in $D_{b,\delta_{0a}} \cap D_{b,\delta_{0b}}$, in which no streamline crossing occurs. Then, as shown above, each of the ξ_i lie on the same streamline, and moreover, each of the Jacobians around the orbit has the form of (2.15). Since the product of such upper triangular matrices with unit entries on the leading diagonal is also an upper triangular matrix with unit entries on the leading diagonal, such a periodic orbit is a parabolic orbit.

In contrast, suppose ξ contains some points which lie in $D_{f,\delta_{0a}} \cup D_{b,\delta_{0b}}$. In this case, computing the product of the Jacobians is not as simple, since we require a coordinate change each time the trajectory changes ρ. In general, this coordinate change will not be analytically tractable, and the eigenvalues of an arbitrary periodic orbit (or trajectory in general) will not be computable. We note that in a related but much simpler system, that of a linked twist map defined on the union of two interlocking circular annuli, the coordinate change can be given explicitly, and the dynamics can be deduced accordingly (Wojtkowski 1980).

In the following, we construct periodic orbits of a given period with the property that all points in the periodic orbit lie in $D_{b,\delta_{0a}} \cap D_{b,\delta_{0b}}$. These parabolic orbits are precisely the points which give rise to large islands appearing in the flow. To simplify the analysis in § 2.3, we remove the arbitrary phase shift from the definition of the map. Then each iteration of the maps P_a and P_b corresponds to a change in angular velocity. The islands in figures 5 and 6 are the islands we construct below, although their positions are rotated. Note that a result of this is that an island may be shifted out of the bulk and into the flowing layer, but this is simply the effect of the phase shift and does not contradict the premise that the large parabolic islands are formed from orbits which do not visit the flowing layer at switching times.

2.3. *Appearance of islands*

It is immediately noticeable that all figures in figure 5 share a common feature. All have prominent islands which lie at approximately the same radial position and are similarly all equally spaced in θ. We first discuss the case of even N. For $m = N/2$ applications of the linked twist map in time $T/2 = \pi$, there are m such islands. The blinking form of the system makes it possible to predict the locations of these islands.

2.3.1. *Even frequency ratios*

Consider a trajectory starting on a closed streamline $\mathscr{S}(r)$ at (x_2, y_2), just entering the bulk. In order for this orbit to be a periodic orbit of period $m = N/2$ it must return to its initial condition after time $T/2$; that is, the distance travelled along $\mathscr{S}(r)$ in time $T/2 = \pi$ must equal the length of $\mathscr{S}(r)$ itself (alternatively, the distance travelled could be an integer multiple of the length of $\mathscr{S}(r)$, but for simplicity we preclude this and concentrate on orbits of minimal period m). For such a periodic orbit to avoid the flowing layer at switching points requires m episodes of angular velocity ω_a interspersed with $m-1$ episodes of angular velocity ω_b occurring whilst the tracer particle remains in the bulk. The remaining episode of angular velocity ω_b must carry the particle from the bulk, through the flowing layer, and back to the bulk. Thus, the aim is to find a streamline $\mathscr{S}(r)$ which makes such an orbit possible.

Radial position of islands. The length l of streamline $\mathscr{S}(r)$ can be given as

$$l(\mathscr{S}(r)) = l(\mathscr{S}_b(r)) + l(\mathscr{S}_f(r)), \tag{2.17}$$

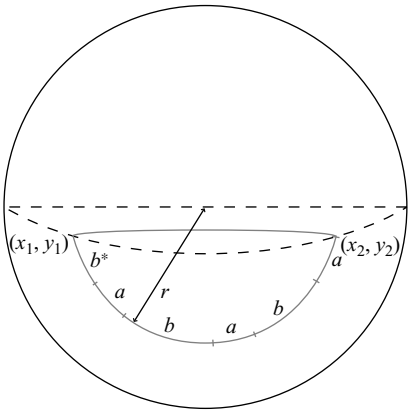

FIGURE 7. Sketch of periodic orbit with the property that switching points do not fall in the intersection of the flowing layers. Here $N = 6$.

where $\mathscr{S}_b$ is the portion of the streamline lying in the bulk, and $\mathscr{S}_f$ is the portion lying in the flowing layer. Since streamlines in the bulk form a circular arc, we have (see figure 7)

$$l(\mathscr{S}_b(r)) = r\left(\pi - 2\sin^{-1}\left|\frac{y_1}{r}\right|\right),$$

where $y_1 = y_2$. Recall that at the boundary of the bulk and the flowing layer,

$$y_1 = \delta_0\sqrt{\frac{L^2 - r^2}{L^2 - \delta_0^2}}.$$

The distance travelled along the closed streamline is given by

$$d(r) = m\frac{\tau}{2}r\omega_a + (m-1)\frac{\tau}{2}r\omega_b + b^* + l(\mathscr{S}_f(r)), \tag{2.18}$$

where b^*, as shown in figure 7, is the remainder of the bulk streamline after time $(N-1)\tau/2$. Equating (2.17) and (2.18), we find that we need r such that

$$r\left(\pi - 2\sin^{-1}\left|\frac{y_1}{r}\right|\right) = m\frac{\tau}{2}r\omega_a + (m-1)\frac{\tau}{2}r\omega_b + b^*. \tag{2.19}$$

Let $t(\mathscr{S}_f(r)$ be the time taken to traverse the flowing layer. In Appendix A we show how to compute this analytically, and give the expression

$$t(\mathscr{S}_f(r)) = \frac{\pi}{\sqrt{\omega_b\dot{\gamma}_b}}.$$

We have

$$b^* = r\omega_b\left(\tfrac{\tau}{2} - t(\mathscr{S}_f(r))\right).$$

Substituting this into (2.19), and since $\bar{\omega} = 1$ implies $\omega_a + \omega_b = 2$, we have

$$r\left(\pi - 2\sin^{-1}\left|\frac{y_1}{r}\right|\right) = m\tau r - r\omega_b t(\mathscr{S}_f(r)))$$

or, since $m\tau = \pi$,

$$2\sin^{-1}\left|\frac{y_1}{r}\right| = \omega_b t(\mathscr{S}_f(r)).$$

Solving the above gives $r \approx 0.5191$. Note that this expression is independent of N, and so we expect the islands in figure 5 to appear at the same radius for each N. The above is valid for m such that $\tau = \pi/m$ is less than $t(\mathscr{S}_f(r))$ (that is, the time between switching points is large enough to allow a particle to pass completely through the flowing layer). This is the case up to (about) $m = 10$.

Angular length of islands. The length b^* gives the angular length of points which have the property of not falling into the flowing layer at a switching point during a complete period. This gives the approximate size and location of islands which should be expected in such a system. Thus since as above $b^* = r\omega_b(\tau/2 - \pi/\sqrt{\omega_b \dot{\gamma}_b})$ whilst crossing the flowing layer at angular velocity ω_b, the sizes of the parabolic islands are determined by the parameters ω_b and $\dot{\gamma}_b$. For example, if $m = 2$, $b^* \approx 0.371$, with the time to cross the flowing layer $t(\mathscr{S}_f(r)) \approx 0.4986$.

Of course, if the slower speed ω_a is such that the time to cross the flowing layer is also less than τ, we can make the same argument as the above with the a and b interchanged (so that we have m episodes at speed ω_b and $m - 1$ episodes at speed ω_a in the bulk, with the flowing layer crossed at speed ω_a). Doing so gives $r \approx 0.5176$ and $a^* \approx 0.1419$, giving the smaller parabolic islands discernible between the larger ones in figure 5.

2.3.2. *Odd frequency ratios*

Figure 6, corresponding to those in Fiedor & Ottino (2005), shows cases for odd values of N. This means that in time $T/2 = \pi$, we have a non-integer number of applications of the linked twist map (recall that $m = N/2$). Thus, we must look for periodic orbits of twice the length – that is, a periodic orbit which returns after time $T = 2\pi$. Applying the above argument (that is, looking for a periodic orbit which makes one circuit of the bulk and flowing layer in time $2T$) leaves the equation

$$r\pi - 2r \sin^{-1} |y_1/r| = m\tau r(\omega_a + \omega_b) - \tau w \omega_b + b^*,$$

that is,

$$\pi + 2 \sin^{-1} |y_1/r| = \omega_b t(\mathscr{S}_f(r)).$$

However, typically, it is not possible to balance this as the time to cross the flowing layer is much too small. We can make a similar argument, however, for a periodic orbit which completes two circuits of the bulk in time T. In this case (taking odd m – for even m one can look at half a periodic orbit and repeat the argument above), we have the distance travelled in time T to be

$$d(r) = (2m-1)r\frac{\tau}{2}\omega_a + (2m-1)r\frac{\tau}{2}\omega_b + a^* + b^* + 2l_f(\mathscr{S}(r),$$

and the length of the streamline as before (to be traversed twice). Thus, we equate

$$2\pi r - 2 \sin^{-1} \left|\frac{y_1}{r}\right|_a - 2 \sin^{-1} \left|\frac{y_1}{r}\right|_b = (2m-1)\frac{\tau}{2} r(\omega_b + \omega_b) + a^* + b^*,$$

that is,

$$2 \sin^{-1} \left|\frac{y_1}{r}\right|_a + 2 \sin^{-1} \left|\frac{y_1}{r}\right|_b = \omega_a t_a(\mathscr{S}_f(r)) + \omega_b t_b(\mathscr{S}_f(r)),$$

where the subscripts a and b denote parameters corresponding to ω_a and ω_b, respectively.

In effect, the difference between even and odd N can be summarized by the fact that for even N, periodic points of period $T/2 = \pi$ are possible, which results in large parabolic islands, whereas for odd N, the shortest period of such periodic points is T.

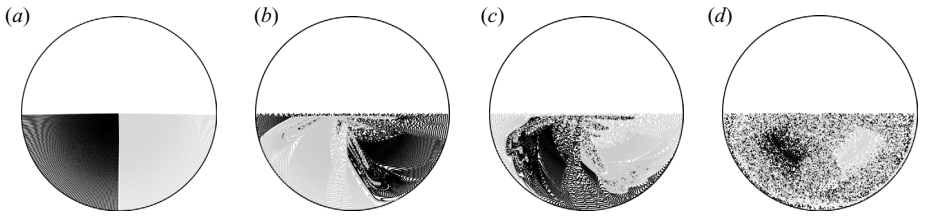

FIGURE 8. Illustration of the dynamical mixing properties of the two-dimensional blinking tumbler for parameter values $\omega_a = 2/3$, $\omega_b = 4/3$, $\delta_{0a} = 0.05$, $\delta_{0b} = 0.1$, $L = 1$ and $N = 4$. The images of the initial black and grey regions shown in (*a*) are shown after 5 iterations in (*b*), 10 in (*c*), and 100 in (*d*).

This is in agreement with the common observation that the largest islands correspond to periodic points with the shortest period.

2.4. *Mixing properties of two-dimensional rotating tumblers*

It is well-known that islands (both elliptic and parabolic) form barriers to mixing in area-preserving dynamics, and that the size of such islands can be gleaned from Poincaré sections such as those in figures 5 and 6. However, Poincaré sections give a picture of the structure of the dynamics only in the limit as time goes to infinity; they do not reveal much information about dynamical mixing properties for finite time.

Figure 8 shows the evolution of two initially separated blobs after 0 (i.e. the initial conditions), 5, 10 and 100 iterations of the map. The parameter values are (as in figures 5 and 6) $\omega_a = 2/3$, $\omega_b = 4/3$, $\delta_{0a} = 0.05$, $\delta_{0b} = 0.1$, $L = 1$, with $N = 4$. We take 10^4 black and 10^4 grey dots and plot their final positions after these numbers of iterations. After 5 and 10 iterations the black and grey are still largely separated, with the boundary between being eroded by lobe-like structures which are typical of the stretching and folding associated with the encroachment of chaotic dynamics. Mixing across the entire domain could be said to be poor, owing to the large unmixed regions of black and grey. After 100 iterations the region is well mixed, with the exception of the rectangular unmixed regions corresponding to the parabolic islands we predict and discuss in § 2.3 (see figure 5 with $N = 4$). It is clear that in spite of the streamline crossing in the system, the mechanism of chaotic mixing is very inefficient, in the sense that mixing in the chaotic sea requires many iterations to be achieved. Although the principles of linked twist map theory described in Sturman *et al.* (2006) do not give any information about the rate at which the mixed state is approached, the inefficiency (both in terms of the number of iterations needed and the spatial extent) of the chaotic mixing mechanism in this two-dimensional system can be understood heuristically: the condition of transversality required by the linked twist map principles is far from being satisfied, which results in inefficient mixing. We are currently working on quantifying the speed of mixing of a linked twist map.

2.5. *Segregation experiments in two dimensions*

It is tempting to think that the best experimental companion to a formalism applied to mixing in granular flows is a mixing experiment: identify a region of particles, distinguishable in some way, for example, by colour, and watch as they mix according to some mixing protocol. However, as indicated in § 1, the reverse is actually true: the simplest experiment, one that can be repeated over and over, is a segregation experiment. The experimental evidence is considerable. Start with two classes of particles and start a mixing protocol; the system will segregate with one class of particles mimicking the placement of islands (Meier *et al.* 2006). We use the linked

twist map formalism on a kinematical model of the flow. Is the underlying flow a good approximation of reality? As we will try to show below, there is a good match between the segregated experimental results and global aspects, such as island placement, predicted by the kinematical model.

Granular materials tend to segregate based on size or density (Hill *et al.* 1999; Duran 2000; Ottino & Khakhar 2000; Ristow 2000). When particles vary in size (S-systems), the small particles segregate from the large particles by percolating in the flowing layer through the interstitial spaces between the large particles (Bridgwater, Sharpe & Stocker 1969; Cantelaube & Bideau 1995; Clément, Rajchenbach & Duran 1995; Dury & Ristow 1997). Percolation results in the small particles drifting to the bottom of the flowing layer, pushing the large particles to the top. When particles vary in density (D-systems), the heavy particles segregate from the light particles in the flowing layer owing to buoyancy differences (Ristow 1994, Jain *et al.* 2005*a*, *b*). The heavy particles sink to the bottom of the flowing layer, pushing the light particles to the top. Once the particles leave the flowing layer, they are fixed in the bed of solid body rotation until they re-enter the flowing layer. When the tumbler has a circular cross-section and the rotation rate is steady, this segregation results in a radial core pattern of small or heavy particles surrounded by large or light particles. However, when the flow is made time-periodic, either through a polygonal tumbler geometry (Hill *et al.* 1999; Cisar *et al.* 2006; Meier *et al.* 2006) or through time-periodic modulation of the rotation rate (Fiedor & Ottino 2005), lobed segregation patterns form. Figures 9 and 10 show segregation patterns formed in half-full quasi-two-dimensional circular tumblers forced with the blinking protocol (equation (2.21)). For even frequency modulation (figure 9), the segregation patterns have lobes that coincide with islands in the corresponding Poincaré sections. We observe pattern capturing for both S-systems (figure 9(ii), (iii)) and D-systems (figure 9(iv)). For odd frequency modulation (figure 10), the connection between the experimental segregation patterns and the computational Poincaré sections is somewhat more complicated.

Segregation based on density can be simulated using a constitutive model for segregation coupled with the continuum equations (equations (2.3)–(2.5)) (Hill *et al.* 1999; Cisar *et al.* 2006) as shown by figure 9(v). The constitutive model treats the two particle types as interpenetrating continua that drift relative to one another until the particle types are segregated into phases rich in each type based on density. In the simulations, the ratio of the minimum to maximum rotation rates is 1:3. The computational patterns shown are formed after 10 tumbler revolutions.

2.5.1. *Experimental details*

The quasi-two-dimensional tumbler is made of acrylic with a diameter of 280 mm and a thickness of 9 mm. The endwalls are made of clear acrylic. The tumbler rotates about its axis, driven with a Parker–Hannifin 34 frame stepper motor. The angular distance, velocity and acceleration are preprogrammed in Visual C++ before being sent by a computer to the motor through an indexer and drive. In the experiments, the minimum rotation rate is 1 r.p.m. (revolutions per minute) and the maximum rotation rate is 3 r.p.m.. Images were taken after 10 tumbler revolutions using a Canon digital camera.

The tumbler is half-filled with the mixture of granular material. In the S-system experiments, the small painted black glass particles are 1.19 ± 0.05 mm in diameter with a density of $2.3\,\mathrm{g\,cm^{-3}}$ and the large clear glass particles are 3.03 ± 0.03 mm in diameter with a density of $2.4\,\mathrm{g\,cm^{-3}}$. In the D-system experiments, the heavy chrome

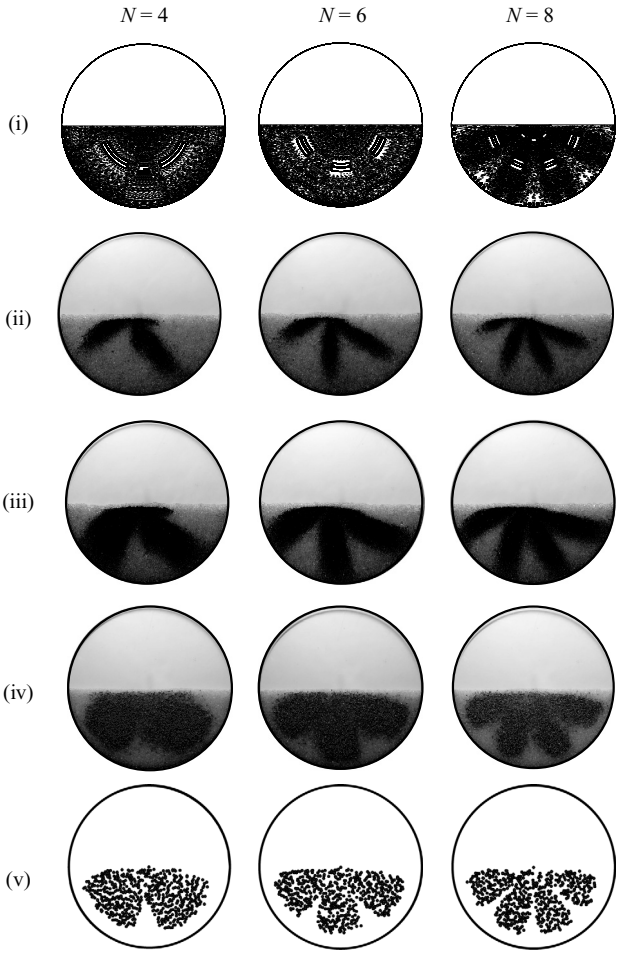

FIGURE 9. Even frequency experimental segregation patterns in two-dimensional systems capture the patterns and symmetries of computational Poincaré sections. (i) Poincaré sections for even frequency modulated tumblers with $N = 4$, 6 and 8. (ii) S-system experiments with a mixture of 10 % by volume small 1 mm painted black glass particles and 90 % by volume 3 mm clear glass particles. (iii) S-system experiments with a mixture of 30 % by volume small 1 mm painted black glass particles and 70 % by volume large 3 mm clear glass particles. (iv) D-system experiments with a mixture of 30 % by volume 2 mm chrome steel beads and 70 % by volume 2 mm clear glass particles. (v) D-system simulations of 600 heavy particles (ratio of particle radius to tumbler radius 1:50).

steel beads are 2.37 ± 0.01 mm in diameter with a density of $7.5\,\mathrm{g\,cm^{-3}}$, and the light clear glass particles are 1.92 ± 0.11 mm with a density of $2.4\,\mathrm{g\,cm^{-3}}$.

2.5.2. *Even frequency modulation*

In figure 9, the small particles (in S-systems) or dense particles (in D-systems) form lobes that coincide with the locations of the islands in the computational Poincaré sections for even frequency modulation. As discussed earlier, even frequency modulation results in $N/2$ islands for half-full tumblers. For $N = 4$, there are two large islands in the Poincaré section and two lobes of small glass particles in the two S-system experimental patterns (10 % by volume small glass particles and 30 % by

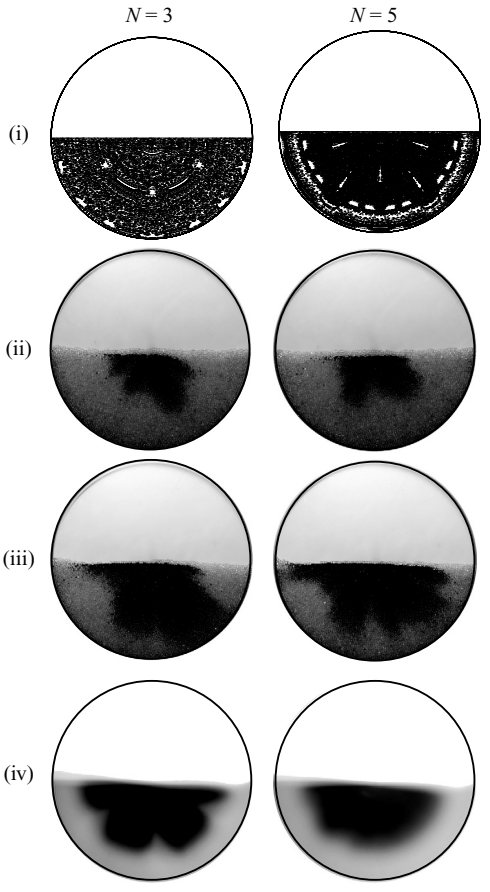

FIGURE 10. Odd frequency experimental segregation patterns do not directly capture the patterns and symmetries of computational Poincaré sections. (i) Poincaré sections for odd frequency modulated tumblers with $N = 3$ and 5. (ii) S-system experiments with 10 % by volume small 1 mm painted black glass particles and 90 % by volume 3 mm clear glass particles. (iii) S-system experiments with 30 % by volume small 1 mm painted black glass particles and 70 % by volume 3 mm clear glass particles. Images in (ii) and (iii) were taken after 10 tumbler revolutions. (iv) Long time averaged segregation experiments. $N = 3$ image includes over 1000 images taken once every half tumbler revolution. $N = 5$ image includes 8700 images taken once every half tumbler revolution.

volume small glass particles). In the D-system experimental pattern (30 % by volume heavy steel particles), two lobes of heavy steel particles are present. For $N = 6$, there are three islands in the Poincaré section and three lobes of small or heavy particles in the segregation patterns. In the $N = 8$ case, there are four islands in the Poincaré section and four lobes of small or dense particles in the segregation patterns.

2.5.3. *Odd frequency modulation*

Interpretation of odd frequency segregation patterns and Poincaré sections is more complicated than that for the even frequency modulation case. As mentioned earlier, the number of large islands in a Poincaré section for odd frequency modulation in a half-full tumbler is N rather than $N/2$. As shown in figure 10(i), the $N = 3$ Poincaré section shows three large islands (two in the bulk located approximately halfway radially between the tumbler centre and the tumbler wall and one in the

flowing layer). The $N = 5$ Poincaré section shows five islands (four in the bulk located approximately halfway radially between the tumbler centre and the tumbler wall and one in the flowing layer). In both Poincaré sections, smaller islands are visible between the tumbler centre and the large islands. In the $N = 3$ case, there is one small inner island. In the $N = 5$ case, there are two small inner islands.

As shown by the S-system results, in figure 10(ii) and (iii), segregation patterns in odd frequency modulated experiments do not form lobes which coincide with the location of islands. In the 10 % by volume small particle experiment (figure 10(ii)) for $N = 3$, there is one large lobe of segregated small particles stretching to the lower right-hand region of the tumbler. Three other small lobes also emerge from the segregated core of small particles. However, in the 10 % by volume small particle experiment for $N = 5$, the segregated small particles appear to form two lobes that coincide with the location of the inner two islands in the $N = 5$ Poincaré section.

At the higher concentration (30 % by volume small particles), shown in figure 10(iii), the segregated small particle pattern for $N = 3$ does not coincide with the location of the parabolic islands in the corresponding Poincaré section. The 30 % small particle pattern is similar to that of the 10 % small particle case with a large lobe stretching toward the bottom right-hand portion of the tumbler. There are two other lobes, one stretching toward the bottom left-hand portion of the tumbler and one in the flowing layer. In the $N = 5$ case, the segregated small particle pattern for 30 % small particles shows several lobes that do not coincide with islands in the corresponding Poincaré section.

These results for odd frequency modulation are similar to observations by Fiedor & Ottino (2005) for sinusoidal forcing. They suggested that lobe formation is reinforced in even frequency modulation, but not in odd frequency modulation. Using long time averaging of images of the segregation pattern obtained over thousands of revolutions, Fiedor & Ottino (2005) captured the lobes in odd frequency segregation patterns. Figure 10(iv) shows the long time averaging result for $N = 3$ and $N = 5$ with the blinking protocol. As shown for $N = 3$, three lobes appear after averaging images taken with a computer-controlled Kodak digital camera once every half revolution for over 500 tumbler revolutions. The locations of the lobes correspond to the locations of the large islands in the $N = 3$ Poincaré section. In the case of $N = 5$, segregation pattern lobes do not appear even after averaging the images taken once every half revolution for over 4300 tumbler revolutions. A radially segregated core is present instead. However, this segregation pattern does capture the overall pattern of the Poincaré section near the five islands. In this case, the five islands are too close together for individual lobes to appear in the segregation pattern.

3. Rotating tumbler mixers in three dimensions

The study of three-dimensional granular mixers is in its early stages. However, it is important to note that one of the most commonly studied granular systems is a three-dimensional long rotating cylindrical tumbler containing a bidisperse size-varying mixture (Hill, Caprihan & Kakalios 1997; Fiedor & Ottino 2003; Khan, Tokaruk & Morris 2004; Khan & Morris 2005). Axial transport in this case produces alternating bands of large and small particles. However, it has been proposed that the axial transport is due to differences between the angles of repose of the different particle types or of mixed and pure phases of particles (Donald & Roseman 1962; Bridgwater *et al.* 1969; Dasgupta, Khakhar & Bhatia 1991) rather than advective axial flow. Measurements of the surface flow in long cylindrical tumblers of monodisperse

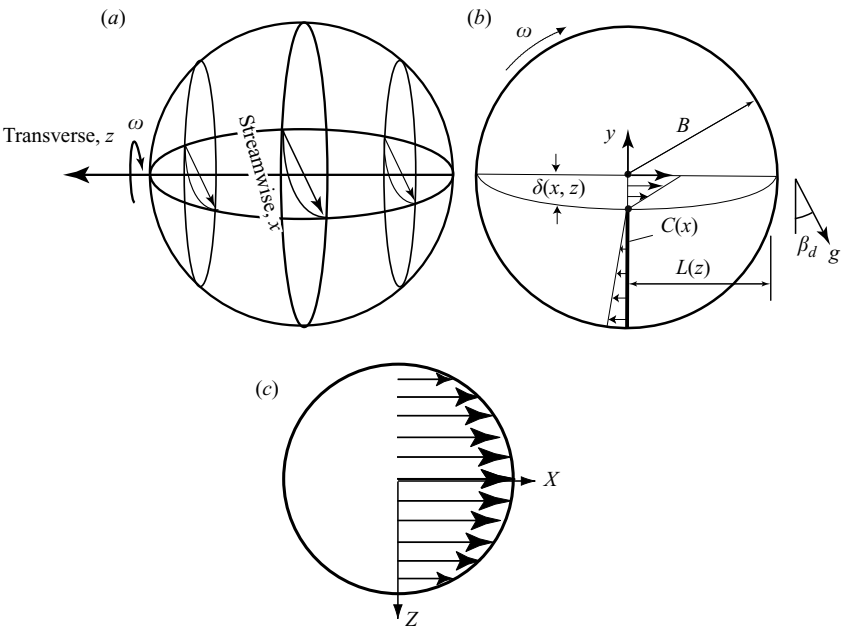

FIGURE 11. (*a*) The rotating spherical tumbler showing the $z =$ constant invariant planes. (*b*) The flow in a $z =$ constant plane and the geometry associated with the construction of action–action–angle variables. (*c*) Top view of the surface velocity profile.

mixtures show that the streamwise velocity at the midlength of the free surface is a linear function of the cross-sectional flowing layer half-length, L (where $L = L(z)$) and that the transverse velocity in the axial direction is negligibly small compared to the streamwise velocity (Pohlman *et al.* 2006*a*). Exceptions occur near the endwalls where endwall friction results in boundary-layer effects (Pohlman *et al.* 2006*b*). This result suggests that the underlying flow in each cross-section of a long rotating tumbler is two-dimensional (neglecting the small endwall regions).

We consider a situation where advective fully three-dimensional flow is generated. Relevant examples come from Elperin & Vikhansky. They proposed a model for flow in an ellipsoidal tumbler rotated about its main axis that is wobbled (Elperin & Vikhansky 2000). Later, they used level-set methods to define the free surface of granular flows in various three-dimensional tumblers (Elperin & Vikhansky 2002). Rocking/rotating cylindrical tumblers have also been studied experimentally by Wightman and colleagues (Wightman *et al.* 1998, 1995; Wightman & Muzzio 1988*a*, *b*) and Fiedor, Umbanhowar & Ottino (2006). A rocking/rotating spherical tumbler was studied experimentally and computationally with a continuum model (Gilchrist & Ottino 2003).

Granular flow in a spherical tumbler is an ideal system for the application of a three-dimensional continuum model because experimental measurements show that the surface flow at the midlength is a linear function of cross-sectional tumbler geometry (Pohlman *et al.* 2006*a*). Since the endwall area goes to zero at the poles of the spherical tumbler, boundary-layer effects that appear in long-rotating cylindrical tumblers are not present. Therefore, the two-dimensional continuum model presented earlier can be applied to these flows treating each cross-sectional slice as an independent two-dimensional flow scaling with the cross-sectional tumbler geometry (figure 11).

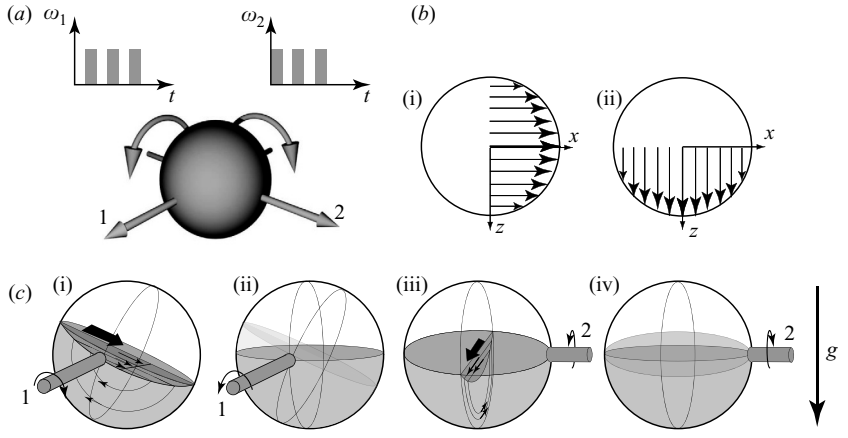

FIGURE 12. (*a*) The blinking protocol for a spherical mixer. Axes 1 and 2 are orthogonal to each other and intersect at the origin of the sphere. (*b*) Top view of the surface velocity profiles due to rotation around (i) axis 1 and (ii) axis 2. (*c*) (i) The flow in a fixed cross-section for clockwise rotation around axis 1. (ii) Reorientation of free surface back to horizontal by gently rotating counterclockwise around axis 1. (iii) The flow in a fixed cross-section for counterclockwise rotation around axis 2. (iv) Reorientation of free surface back to horizontal by gently rotating clockwise around axis 2.

3.1. *Spherical tumbler mixers with constant angular velocity*

Three-dimensional granular tumblers, and in particular spherical tumblers were analysed in Pohlman *et al.* (2006*a*). Here we present the continuum model for granular flow in the continuous-flow (rolling) regime in a spherical tumbler rotated about two orthogonal axes labelled 1 and 2 in figure 12(*a*). A thorough derivation of the continuum model for this case is presented in Meier *et al.* (2007).

3.1.1. *Rotation about axis 1*

In this section, we extend the system defined in § 2 to the case of three-dimensional flow in a half-full sphere of radius R rotating at a constant rate, ω_1, about axis 1 with flow in a rapidly flowing free-surface layer orthogonal to the axis of rotation and at an angle with respect to the horizontal (defined by the 1,2 plane) referred to as the dynamic angle of repose. The coordinate system of the flow in the case of rotating about axis 1 is defined with the direction of flow labelled as the x-direction with the transverse direction labelled as the z-direction (parallel to axis 1) as shown in figure 12(*b*) (i). The key assumption here is that particles have no velocity component parallel to the axis of rotation. Thus in Cartesian coordinates, the velocity components of particles in the bulk (bed of solid-body rotation) are given by

$$\dot{x} = \omega_1 y = \frac{\partial \psi_b}{\partial y},$$
$$\dot{y} = -\omega_1 x = -\frac{\partial \psi_b}{\partial x},$$
$$\dot{z} = 0,$$

where

$$\psi_b = \frac{1}{2}\omega_1 (x^2 + y^2).$$

As in the two-dimensional case, particles are exchanged between the bulk (bed of solid-body rotation) and a rapidly flowing free-surface layer. In the flowing layer, the streamwise (positive x-direction) velocity varies linearly with depth in the layer with a maximum at the free surface. The linear variation with depth or shear rate, $\dot{\gamma}_1$, is taken as constant with respect to the streamwise position, $\dot{\gamma}_1 \neq \dot{\gamma}_1(x)$. In this case, the shape of the flowing layer is given in Cartesian coordinates with the origin centred at the midpoint between the tumbler walls in the direction of flow (that is, at the centre of a half-full sphere) by:

$$\delta_1(x, z) = \delta_0\sqrt{1 - \frac{x^2}{L^2}} = \sqrt{\frac{\omega_1}{\dot{\gamma}_1}}\sqrt{R^2 - x^2 - z^2}, \tag{3.1}$$

since we have $L = L(z) = \sqrt{R^2 - z^2}$ and $\delta_0 = \sqrt{\omega_1/\dot{\gamma}_1}L(z)$ (recall § 2.1).

The velocity field in the flowing layer is given by

$$\begin{aligned}
\dot{x} &= \dot{\gamma}_1\left(\delta_1(x, z) + y\right) = \frac{\partial \psi_f}{\partial y}, \\
\dot{y} &= \frac{\omega_1\, x\, y}{\delta_1(x, z)} = -\frac{\partial \psi_f}{\partial x}, \\
\dot{z} &= 0,
\end{aligned}$$

where

$$\psi_f = \dot{\gamma}_1\left(\delta_1(x, z)y + \tfrac{1}{2}y^2\right). \tag{3.2}$$

3.1.2. *Rotation about axis 2*

We will be interested in alternating rotation at constant velocity about two different axes (figure 12*a*). For clarity, we give here the equations of motion for rotation at rate ω_2 about axis 2. For rotation about axis 2, the direction of flow is labelled by the positive z-direction (at an angle with respect to the horizontal defined by the 1,2 plane) and the transverse direction is labelled by the x-direction (parallel to axis 2). The boundary of the flowing layer is given by

$$\delta_2(x, z) = \sqrt{\frac{\omega_2}{\dot{\gamma}_2}}\sqrt{R^2 - x^2 - z^2}.$$

Note that if $\omega_1/\dot{\gamma}_1 = \omega_2/\dot{\gamma}_2$ then $\delta_1(x, z) = \delta_2(x, z)$. In the bulk, we have the velocity field

$$\begin{aligned}
\dot{x} &= 0, \\
\dot{y} &= -\omega_2 z = -\frac{\partial \psi_b}{\partial z}, \\
\dot{z} &= \omega_2 y = \frac{\partial \psi_b}{\partial y},
\end{aligned}$$

where

$$\psi_b = \tfrac{1}{2}\omega_2(y^2 + z^2),$$

while in the flowing layer the motion is described by

$$\begin{aligned}
\dot{x} &= 0, \\
\dot{y} &= \frac{\omega_2\, z\, y}{\delta_2(x, z)} = -\frac{\partial \psi_f}{\partial z}, \\
\dot{z} &= \dot{\gamma}_2\left(\delta_2(x, z) + y\right) = \frac{\partial \psi_f}{\partial y},
\end{aligned}$$

where the streamfunction in the flowing layer for the flow generated by rotation about axis 2 is that corresponding to the streamfunction in the flowing layer generated by rotation about axis 1 (equation (3.2)), i.e.

$$\psi_f = \dot{\gamma}_2 \left(\delta_2(x, z)y + \tfrac{1}{2}y^2\right).$$

In between rotating around each of the axes, we reorient the free surface back to parallel with the 1,2 plane, as shown in figure 12(*c*). This eliminates complications associated with the free surface being at an angle with respect to the 1,2 plane at the beginning of each of the flows. With the reorientations, the flows can be considered as maps owing to rotations with respect to the z-axis and x-axis. To simplify the discussion from this point on, we refer to rotations with respect to the z- and x-axes.

3.1.3. *Characterizing particle kinematics by a three-dimensional twist map: action–action–angle variables for the spherical tumbler rotating with constant velocity about an axis*

For constant rotation rate about a fixed axis (which we will take as the z-axis for definiteness), we can construct a three-dimensional generalization of action–angle variables, which we refer to as *action–action–angle* variables (see Mezic & Wiggins 1994), in which the velocity field takes a simple form and leads to a straightforward analysis of the kinematics of particle trajectories. The key connection to the two-dimensional setting comes from noting that since $\dot{z} = 0$, the flow occurs entirely in the planes $z =$ constant. Therefore, in each such plane we can transform to action–angle variables using the standard two-dimensional coordinate transformation derived in § 2.1.1, and the 'second action' is the coordinate z.

In order to describe the *global streamfunction* we must define carefully the domains of the two different flows. The flowing layer is defined by:

$$D_{f,\delta_0} = \{(x, y, z) \,|\, -R \leqslant x \leqslant R,\ -R \leqslant z \leqslant R,\ 0 \leqslant y < -\delta(x, z)\},$$

where the thickness of the flowing layer is given by (3.1). Outside the flowing layer, the particles undergo solid-body rotation. We refer to this region as 'the bulk', and it is defined by:

$$D_{b,\delta_0} = \{(r, \theta, z) \,|\, 0 \leqslant r \leqslant R,\ 0 \leqslant \theta < \pi,\ -R \leqslant z \leqslant R\} - D_{f,\delta_0}.$$

The boundary between D_{f,δ_0} and D_{b,δ_0}, denoted $\partial_{f,b}$ is therefore given by

$$\partial_{f,b} = \{(x, y, z) \,|\, -R \leqslant x \leqslant R,\ y = -\delta(x, z),\ -R \leqslant z \leqslant R\},$$

and the domain of the flow is $D_{f,\delta_0} \cup D_{b,\delta_0}$. We define the flow on each region separately, and a matching condition for the streamlines at the boundary in exactly the same way as described following equation (2.9), giving the streamfunction

$$\psi(x, y, z) = \begin{cases} \psi_f(x, y, z) & \text{on} \quad D_{f,\delta_0}, \\ \psi_b(x, y) & \text{on} \quad D_{b,\delta_0}. \end{cases}$$

As before, we can define the transformation to the action, action and angle coordinates, and describe their relationship to the geometry of closed streamlines in $z =$ constant planes. Let $C(z)$ denote a reference curve on the $z =$ constant plane which is a straight line connecting $(0, -\delta_1(0, z), z)$ to $(0, -L, z) = (0, -\sqrt{R^2 - z^2}, 0)$ (see figure 11*b*). $C(z)$ will be the starting point of trajectories on the $z =$ constant plane. We represent $C(z)$ in parametric form as follows:

$$C(z) = \{(0, y_0(z), z) \in \mathbb{R}^3 \mid -\delta_1(0, z) \geqslant y_0(z) \geqslant -L\},$$

and trajectories starting on $C(z)$ by $(x(t,z), y(t,z), z)$ where $x(0,z)=0$ and $y(0,z)=y_0(z)$. Let (x, y, z) be an arbitrary point on a closed streamline traced out by the trajectory $(x(t,z), y(t,z), z)$ and let $t=t(x, y, z)$ be the time taken for the trajectory starting at $(0, y_0(z), z)$ to flow to (x, y, z). We denote the period of each closed trajectory on a $z=$constant plane defined by $\psi(x, y, z)=\psi=$constant by $T(\psi, z)$. The *angle variable* on the $z=$constant plane, $\phi(x, y, z)$, is now defined as:

$$\phi(x, y, z) = \frac{2\pi}{T(\psi, z)} t(x, y, z),$$

where $(x, y, z) \in \psi=$constant.

The area enclosed by any closed streamline in the $z=$ constant plane is clearly constant in time (since $\dot{z}=0$). This is used to define one *action variable*, denoted $\rho(z)$, as:

$$\rho(z) = \frac{1}{2\pi} \oint_{\psi} x \, \mathrm{d}y, \tag{3.3}$$

where ψ labels the closed streamline in the $z=$ constant plane defined by $\psi(x, y, z)=\psi=$constant. Just as in the two-dimensional situation, it should be clear from (3.3) that the action variable for a closed streamline is a function of ψ, which we explicitly denote as:

$$\rho(z) = \rho(\psi, z),$$

and that this relationship can be inverted (for z held constant) as a result of the one-to-one relationship between closed streamlines and the area they enclose:

$$\psi = \psi(\rho, z).$$

We can also label the period of each closed streamline in a $z=$ constant plane by either ρ or ψ.

In summary, we have defined coordinates (ρ, ϕ, z) on a region of closed streamlines on any $z=$ constant plane such that the velocity field is given by

$$\left.\begin{aligned} \dot{\rho} &= 0, \\ \dot{\phi} &= \frac{2\pi}{T(\rho, z)} \equiv \Omega(\rho, z), \\ \dot{z} &= 0, \end{aligned}\right\} \tag{3.4}$$

where $\Omega(\rho, z)$ is the frequency associated with the closed streamline having action ρ in the $z=$ constant plane. The trajectories of (3.4) are easily obtained as:

$$\left.\begin{aligned} \rho(t) &= \rho_0 = \text{constant}, \\ \phi(t) &= \frac{2\pi}{T(\rho, z)} t + \phi_0 \equiv \Omega(\rho, z)t + \phi_0, \\ z(t) &= z_0 = \text{constant}. \end{aligned}\right\} \tag{3.5}$$

The same argument given in Wiggins (2003) for the two-dimensional case shows that restricted to a $z=$ constant plane, the Jacobian of the transformation (with respect to x and y) to action–angle coordinates is identically one, which implies that area is preserved under the action–angle transformation, and that the 'Hamiltonian structure' (with respect to the x and y coordinates) is also preserved under action–angle transformations. This latter point means that if we take the streamfunction in the original (x, y, z) coordinates and transform the x and y components to action–angle

coordinates, then the velocity field in action–action–angle coordinates is obtained from this transformed streamfunction in the usual way. More importantly, the transformed streamfunction is a function of just the ρ and z variables.

As in the two-dimensional case, we consider the motion of particles in terms of a map. The map is constructed from the trajectories (3.5), and is obtained by considering the evolution of particles for a fixed interval of time, which we will take to be $t = \tau_1$. Therefore, the mapping of points is given by

$$P(\rho, \phi, z) = (\rho, \phi + \Omega(\rho, z)\tau_1, z)\,.$$

This is a three-dimensional generalization of a twist map since the $\Omega(\rho, z)$ is a monotonic function of ρ, for each fixed z, which is responsible for shearing, or 'twisting' of a line of initial conditions transverse to the streamlines. These types of maps, subject to perturbations, have been studied in Wiggins & Holmes (1987), Mezic & Wiggins (1994) and Mezic (2001).

3.2. *Alternating axes of rotation: the blinking spherical tumbler as a three-dimensional linked twist map*

A three-dimensional blinking mixer can be created by alternating rotation about axis 1 with rotation about axis 2. It is important to note that the free surface is parallel to the horizontal at the beginning of each rotation. For example, after generating the flow due to rotation around axis 1 (figure 12*c*(i)), the free surface is brought back to parallel with the horizontal by gently rotating the tumbler without generating surface flow in reverse around axis 1 (figure 12*c*(ii)) before rotating the tumbler around axis 2 (figure 12*c*(iii)). Similarly, after generating the flow due to rotation around axis 2, the free surface is brought back to parallel with the horizontal by gently rotating the tumbler in reverse around axis 2 (figure 12*c*(iv)) without generating surface flow before rotating the tumbler around axis 1. As mentioned at the end of § 3.1.2, by reorienting the free surface back to horizontal between rotations on each axis, the flows can be considered as maps due to rotations with respect to the z- and x-axes.

In terms of action–action–angle coordinates, the blinking spherical mixer can be described as a linked twist map by the composition of the map

$$P_x(\rho_x, \phi_x, z) = (\rho_x, \phi_x + \Omega_x(\rho_x, z)\tau_1, z),$$

which represents rotation about the z-axis with frequency Ω_x, and the map

$$P_z(x, \rho_z, \phi_z) = (x, \rho_z, \phi_z + \Omega_z(\rho_z, x)\tau_2),$$

which represents rotation about the x-axis with frequency Ω_z. As for the two-dimensional blinking tumbler, to formally compose these maps we require a nonlinear change of variable transformation $\mathscr{V}$ to write the linked twist map $\mathscr{Q}$ as

$$\mathscr{Q} = \mathscr{V}^{-1} \circ P_z \circ \mathscr{V} \circ P_x. \tag{3.6}$$

3.3. *Dynamical properties of the three-dimensional linked twist map*

Now we begin our studies of the mixing properties of the blinking spherical tumbler by studying the dynamics of the associated three dimensional linked twist map. We begin by stating some very general results, with the details relegated to appendices.

THEOREM 3.1. *The integrable twist map P_x has a surface of period-one points in the bulk, Σ_1, having the form of a 'bowl' which is part of a prolate spheroid (see figure 13), with the semi-major axis parallel to the z-axis. Similarly, the integrable twist map P_z*

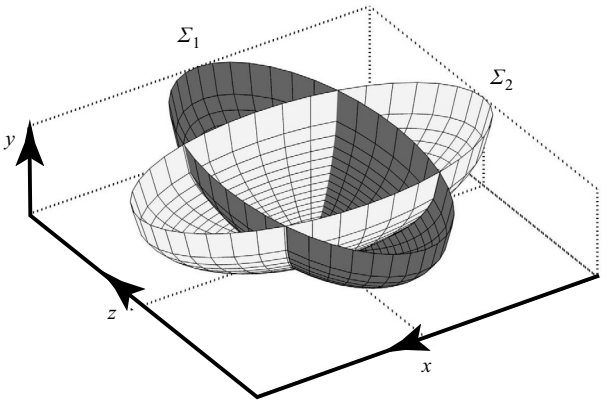

FIGURE 13. The intersecting prolate spheroids Σ_1 and Σ_2.

also has a surface of period-one points in the bulk, Σ_2, having the form of a bowl which is also part of a prolate spheroid, with the semi-major axis parallel to the x-axis. The surfaces Σ_1 and Σ_2 intersect in four curves which are period-one points for the linked twist map $\mathcal{Q}$. Moreover, these curves alternate in stability type, with two being normally elliptic and two being normally hyperbolic.

Details of the proof of this result are given in Appendices C, D and E. We note that it is shown in Appendix C that these spheroids are completely defined in terms of the parameters ω_1, ω_2, $\dot{\gamma}_1$, $\dot{\gamma}_2$, R, τ_1 and τ_2. In general, period-one points are significant because they give rise to the largest islands, i.e. regions of fluid that do not mix with the surroundings. In this three-dimensional setting, we see something different: 'islands' whose 'centres' are not elliptic periodic points, but normally elliptic invariant curves. These normally elliptic invariant curves are surrounded by 'KAM tubes', which are barriers to mixing. The normally hyperbolic invariant curves have two-dimensional stable and unstable manifolds (Wiggins 1994). More background on the implications of these three-dimensional structures on mixing can be found in Mezic & Wiggins (1994), but we emphasize that these types of three-dimensional structures have received little attention in realistic examples.

If the ratio of angular rotation rate to shear rate is the same for both rotations, particle trajectories are constrained to a single surface that depends on the initial condition, and transport throughout the entire hemispherical domain does not occur. More interesting dynamics, and in particular transport throughout the hemisphere, will be possible if the rotations have different angular velocities. Here, we state the result where particles are constrained to lie on a fixed surface (depending on the initial condition of the particle).

THEOREM 3.2. *The motion of a particle acting under rotations about the z- and x-axis alternately, when $\omega_1/\dot{\gamma}_1 = \omega_2/\dot{\gamma}_2$, is constrained to a single surface, determined by the initial position of the particle, given by a hemispherical bowl formed from paths through the bulk, with a 'lid' formed from paths through the flowing layer. In particular, this result is not dependent on the amount of time for which each rotation acts.*

This theorem effectively follows from the fact that if $\omega_1/\dot{\gamma}_1 = \omega_2/\dot{\gamma}_2$, then $\delta_1(x, z) = \delta_2(x, z)$, which gives a symmetry to the flowing-layer dynamics. The details of the proof are given in Appendix B.

3.4. *The symmetric case*

In the case that $\omega_1 = \omega_2$ and $\dot{\gamma}_1 = \dot{\gamma}_2$, theorem 3.2 shows that the dynamics is constrained to a single hemispherical surface, dependent on the initial condition. Properties of the dynamics within that surface can be found by considering periodic points of the map. Consider the map $P_x(\rho_x, \phi_x, z) = (\rho_x, \phi_x + \Omega_x(\rho_x, z)\tau_1, z)$, the time-$\tau_1$ map of rotation with respect to the z-axis. A period-one point for P_x is a point which returns after one iteration of P_x, that is, a point whose period in the flow is τ_1. In Appendix C, we compute this period analytically. This shows that period-one points lie on the surface Σ_1 given by

$$\Sigma_1 : x^2 + y^2 + c_1 z^2 = c_2,$$

where c_1 and c_2 are constants, $c_1 = c_1(\omega_1, \dot{\gamma}_1, \tau_1)$ and $c_2 = c_2(R, \omega_1, \dot{\gamma}_1, \tau_1)$ given explicitly in Appendix C. Similarly, period-one points for the map $P_z(x, \rho_z, \phi_z) = (x, \rho_z, \phi_z + \Omega_z(\rho_z, x)\tau_2)$ lie on the surface Σ_2 given by

$$\Sigma_2 : c_3 x^2 + y^2 + z^2 = c_4,$$

where c_3 and c_4 are constants, $c_3 = c_3(\omega_2, \dot{\gamma}_2, \tau_2)$ and $c_4 = c_4(R, \omega_2, \dot{\gamma}_2, \tau_2)$. Two such surfaces (prolate spheroids) are shown in figure 13. Period 1 points of the linked twist map $\mathcal{Q}$ are thus given by the intersection of Σ_1 with Σ_2, given by $\Delta = \Sigma_1 \bigcap \Sigma_2$. When $\tau_1 = \tau_2$ there is a further symmetry relating Σ_1 to Σ_2, and Δ consists of a pair of curves $\Delta_{xz>0}$ and $\Delta_{xz<0}$ which intersect at $x = z = 0$. In this case, $c_1 = c_3 = \bar{c}$ and $c_2 = c_4 = \hat{c}$. See Appendix D for details. The stability of these period-one points can be determined by a symmetry argument, detailed in Appendix E. We have that $\Delta_{xz>0}$ is a curve of unstable (hyperbolic) points (i.e. a normally hyperbolic invariant curve), while $\Delta_{xz<0}$ is a curve of stable (elliptic) points (i.e. a normally elliptic invariant curve).

The main features of the dynamics are thus given by the intersection of the invariant hemisphere $\mathcal{H}_r : x^2 + y^2 + z^2 = r^2$ with Δ. In figure 14, we show orbits of 10^4 iterations of carefully chosen initial conditions to illustrate the different possible dynamics. In each of these figures, we plot only those iterations for which $y < -\delta(x, z)$ (i.e. we do not plot points in the flowing layer), and we show the image as a projection in (x, z)-space (effectively looking at the hemisphere from below). The parameter values are $\omega_1 = \omega_2 = 0.5$, $\dot{\gamma}_1 = \dot{\gamma}_2 = 50.0$, $\tau_1 = \tau_2 = 6.0$, $R = 1$. If r is sufficiently small, or sufficiently large, the intersection $\mathcal{H} \cap \Delta$ is empty. In this case, there are no period-one periodic points, and the dynamics has no significant islands. Such dynamics are shown in figures 14(a) and 14(f), for $r = 0.1$ and $r = 0.8$, respectively. The lowest point of Σ_1 and Σ_2 (that is, $\Delta_{xz>0} \cap \Delta_{xz<0}$) occurs at $(x, y, z) = (0, -\sqrt{c_2} = -0.16222, 0)$. Thus when $r = 0.16222$, $\mathcal{H}_r$ touches Δ tangentially. At this point, the period-one point is a parabolic point. This behaviour is shown in figure 14(b). As r increases from this point, $\mathcal{H} \cap \Delta$ has four points, a pair of elliptic points and a pair of hyperbolic points. Two examples of such dynamics are shown in figures 14(c) and 14(d), for $r = 0.18$ and $r = 0.2$, respectively. Finally, figure 14(e) shows the dynamics when the periodic points have reached the boundary of $\mathcal{H}$. This occurs when $r = 2\bar{c}/(1 + \hat{c}) \approx 0.279$.

3.5. *Experiments in three dimensions*

The physics operating in experiments in three dimensions is the same as in two dimensions. There are some experimental difficulties, however, with respect to comparison with the two-dimensional case. The most important is that in two-dimensional experiments, visualization is easy, but not so in three dimensions owing to the

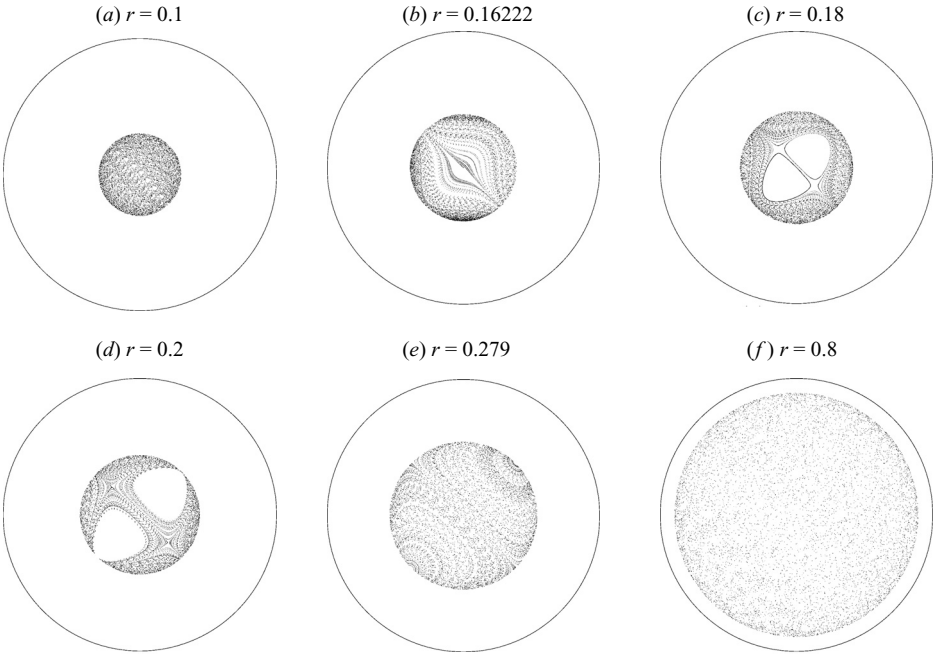

FIGURE 14. Dynamics of the three-dimensional blinking spherical mixer. We plot 10^4 iterations of a single initial condition in each figure. For clarity we plot a plan view and plot only iterations in the bulk. Parameter values are $\omega_1 = \omega_2 = 0.5$, $\dot{\gamma}_1 = \dot{\gamma}_2 = 50.0$, $\tau_1 = \tau_2 = 6.0$, $R = 1$. Since the parameters are the same for each rotation, the dynamics is constrained to a hemispherical surface $x^2 + y^2 + z^2 = r^2$. The particular hemispherical surface is chosen by the initial condition.

non-transparency of granular materials. The interior of three-dimensional systems can be examined using several techniques such as MRI (Nakagawa *et al.* 1993; Metcalfe & Shattuck 1996; Fukushima 1999). Such techniques are still not routine and here we resort to other methods.

In the three-dimensional experiment presented here, tracer particles are advected by the flow. The resulting pattern reveals the dynamics of the underlying flow. The spherical tumbler is made of clear acrylic with a radius of 68 mm. The tumbler is half-filled with granular material. The fluorescent yellow tracer particles (which appear pale grey in figure 15) are 1.94 ± 0.11 mm painted glass particles (density of $2.3\,\mathrm{g\,cm^{-3}}$), while the bulk particles are 1.07 ± 0.04 mm black basalt glass particles (density of $2.6\,\mathrm{g\,cm^{-3}}$). This mixture has a dynamic angle of repose of approximately 26°. The tumbler rotates about two axes driven by Compumotor 34 frame stepper motors. Angular distance, velocity and acceleration are preprogrammed in Visual C++ and sent by a computer to the motors via an indexer and drives. The angular velocity is 2 r.p.m.. The experimental images shown in figure 15(*c*) were taken using a Canon digital camera.

As shown in figure 15, experiments reveal the hemispherical dynamics predicted by the three-dimensional continuum model. In this example, the following protocol is used. First, the tumbler rotates until the surface flow begins and then rotates one full rotation clockwise around axis 1 resulting in flow in the flowing layer in the positive x-direction. The flow is considered steady after 12° of tumbler rotation (Pohlman *et al.* 2006*a*). The flow in the surface layer occurs at an angle to the horizontal, the dynamic angle of repose. Once the full rotation around axis 1 is complete, the tumbler

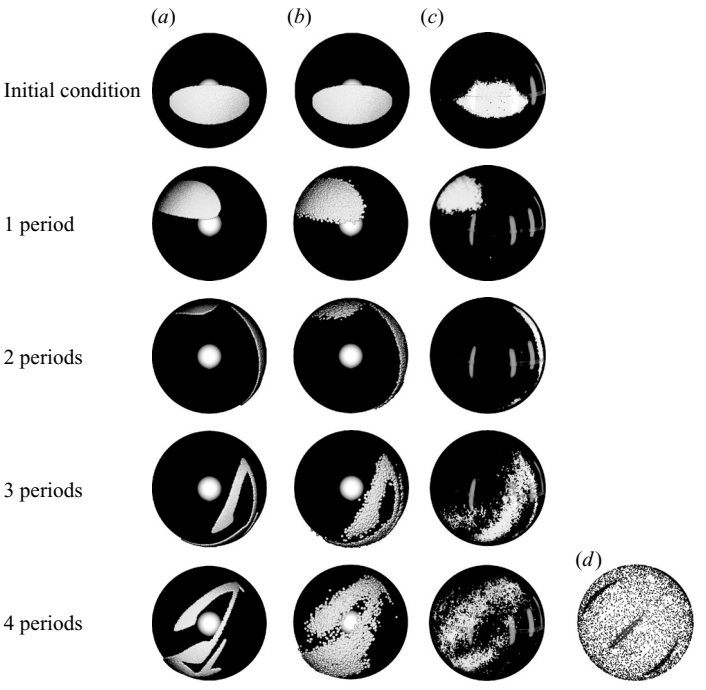

FIGURE 15. Comparison of a simulation using the three-dimensional continuum model without and with diffusion and an experiment. In both the simulation and experiment, tracer particles (appearing grey) are seeded in a blob at the bottom of a half-full spherical tumbler. In all cases, the spherical tumbler is viewed from the bottom. (*a*) The evolution of the pattern over four periods of the two-axis protocol using the continuum model without diffusion. (*b*) The evolution of the pattern over four periods of the two-axis protocol using the continuum model with diffusion added to the velocity equations in the flowing layer in both the x- and z-directions. (*c*) The experimental result of a half-full sphere containing 1 mm black basalt glass particles and 2 mm fluorescent yellow (appearing pale grey) glass tracer particles. (*d*) The corresponding Poincaré section for the three-dimensional flow. It is plotted for 500 periods, with the initial condition consisting of 19 points located in the $x = -z$ plane at $r = 0.95R$. The first three columns of this figure are adapted with permission from Meier *et al.* (2007, © 2007 Taylor & Francis).

is gently rotated counterclockwise around axis 1 to bring the free surface back to horizontal. Next, the tumbler rotates until the surface flow begins and then rotates one full rotation counterclockwise around axis 2 resulting in flow in the flowing layer in the positive z-direction. Finally, the tumbler is gently rotated clockwise around axis 2 to bring the free surface back to horizontal. The protocol then repeats.

For the computational results shown in figure 15(a, b), the shear rate is matched to that for the experiment ($\dot{\gamma} = 50|\omega|$) (Pohlman *et al.* 2006*a*). The hemisphere of interest in figure 15 is close to the tumbler wall ($r = 0.95R$) so that a visual comparison can be made between the computational results and the experimental patterns. While the medium is assumed to be monodisperse in the continuum model simulation, two slightly different sized particles are used in the experiment. By using tracer particles larger than the bulk particles, the tracer particles preferentially occupy the uppermost portion of the flowing layer. When particles in the uppermost portion of the flowing layer enter the bed of solid-body rotation, they reside in the outermost portion near the tumbler wall (outermost hemisphere). (See Clément *et al.* (1995) and Duran (2000)

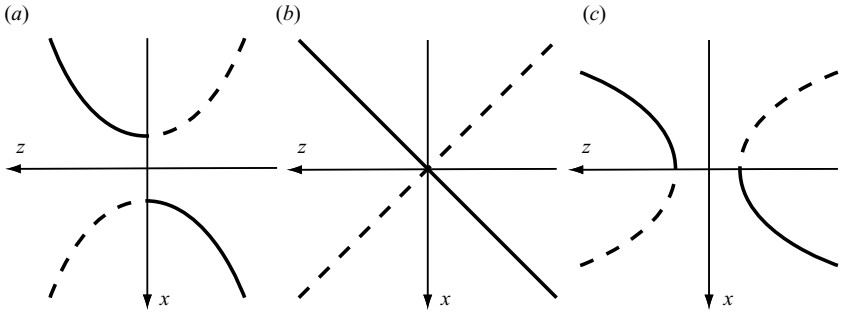

FIGURE 16. Sketch of the intersection of the prolate spheroids $\Sigma_1 \cap \Sigma_2$ in x, z space. (*a*) $\tau_1 > \tau_2$. (*b*) $\tau_1 = \tau_2$. (*c*) $\tau_1 < \tau_2$.

for similar experiments in quasi-two-dimensional tumblers.) If the tracer particles and the bulk particles were exactly the same size and density, the tracer particles would diffusively move through the depth of the flowing layer and may not appear on the outermost hemisphere near the tumbler wall, making visualization of the dynamics near the tumbler wall difficult. As shown by the comparison between the model and experimental results, the continuum model simulation provides an accurate representation of the dynamics of the mixing, particularly when the simulation includes diffusion in both the x- and z-directions in the flowing layer. The chaotic dynamics are evident in the stretching and folding of the 'blob' of tracer particles as evident after three periods of the protocol. Moreover the fold created has a strong correlation with the location of an island in the Poincaré section shown in figure 15(*d*). Note that according to the analysis of § 3.4 we have, for these parameter values, $c_1 = c_2/R^2 \approx 0.021$. This implies there is no intersection between Δ and the hemisphere $r = 0.95R$, and so the visible islands are not period-one islands.

3.5.1. *Non-symmetric cases*

The simplest way to break the symmetry of Σ_1 and Σ_2 is by allowing $\tau_1 \neq \tau_2$, whilst retaining $\omega_1 = \omega_2$ and $\dot{\gamma}_1 = \dot{\gamma}_2$. In this case, theorem 3.2 still applies, and dynamics are still constrained to a hemisphere, but now the intersection Δ need not be a pair of intersecting lines. Instead, the intersection forms a pair of curves (details given in Appendix D) which depend on c_1, c_2, c_3 and c_4. These curves are hyperbolas, with the direction of the semi-major axis depending on the sign of $c_2 - c_4$. Figure 16 shows a sketch in (x, z)-space of the intersection Δ. Figure 16(*a*) shows the situation for $\tau_1 > \tau_2$, which gives Δ to be the hyperbolas $x^2(1 - c_3) + z^2(c_1 - 1) = (c_2 - c_4)$, where $1 - c_3 > 0$, $c_1 - 1 < 0$ and $c_2 - c_4 > 0$. Stable (elliptic) points are shown as a solid line and unstable (hyperbolic) points are shown as a dotted line. Figure 16(*b*) shows the symmetric case $\tau_1 = \tau_2$ discussed above, in which Δ forms the straight lines $x = \pm z$. Finally, in figure 16(*c*), we have $\tau_1 < \tau_2$ and Δ is the hyperbolas $x^2(c_3 - 1) + z^2(1 - c_1) = (c_4 - c_2)$, where $c_3 - 1 < 0$, $1 - c_1 > 0$ and $c_4 - c_2 > 0$. In the language of dynamical systems, these figures could be described as a pair of saddle-node bifurcations (figure 16*a*) approaching each other as τ_1 approaches τ_2 from above, passing through a transcritical bifurcation (figure 16*b*) as $\tau_1 = \tau_2$, and a pair of saddle-node bifurcations separating (figure 16*c*) as τ_1 decreases away from τ_2.

The symmetry of the system could also be broken by allowing $\omega_1 \neq \omega_2$. In this case, periodic points are still given by the intersection of Σ_1 with Σ_2, but for general points, theorem 3.3 does not apply, and so trajectories are not restricted to a single

invariant hemispherical surface. Several questions are immediately raised, which we choose not to address in the present paper. For example, how can the behaviour in the vicinity of a periodic point best be characterized and observed? What is the effect of breaking the symmetry on transport throughout the hemisphere? What are the consequences of this for the mixing properties of the system? How is segregation affected?

3.6. *The $\delta \to 0$ limit*

The limit of a flowing layer of zero width allows us to make connections with some interesting mathematical tools and formalisms in the area of piecewise isometries. This allows us to understand a fundamental difference between granular mixing in two and three dimensions. We first begin by explaining the physical meaning of this limit.

Consider a half-full circular tumbler of radius R rotating at a rate ω. According to the continuum model, a particle on the free surface of the flowing layer experiences a streamwise velocity as a function of its streamwise position, x, given, using (2.4), by

$$u_{surf}(x) = \sqrt{\omega\dot{\gamma}}\sqrt{R^2 - x^2}.$$

where $\dot{\gamma} = \omega R^2/\delta_0^2$ is the shear rate or variation of the streamwise velocity with depth in the flowing layer. The average velocity this particle will experience while travelling the full length of the surface of the flowing layer is given by

$$u_{surf}^{av} = \frac{1}{2R}\int_{-R}^{R} u_{surf}(x)\,\mathrm{d}x = \frac{\pi R}{4}\sqrt{\omega\dot{\gamma}}.$$

In the bulk, a particle that was on top of the free-surface will reside against the tumbler wall. The velocity in the bulk is given by

$$v_\theta = \omega.$$

The time the particle spends in the free-surface flow is given by $2R/u_{surf}^{av}$, while the time spent in the bulk is given by $-\pi/v_\theta$:

$$\frac{\text{Time in flowing layer}}{\text{Time in bulk}} = \frac{8}{\pi^2}\sqrt{\frac{\omega}{\dot{\gamma}}}.$$

As the ratio of the shear rate to the rotation rate becomes very large, the ratio of the time spent in the flowing layer to the time spent in the bulk becomes very small. In the limit $\dot{\gamma}/\omega \to \infty$ (recalling that $\dot{\gamma}/\omega = R^2/\delta_0$ means that this limit is equivalent to $\delta_0 \to 0$), the ratio of the time spent in the flowing layer to the time spent in the bulk goes to zero.

3.6.1. *Piecewise isometries*

Investigating the behaviour of the three-dimensional system in the limit as $\delta \to 0$ is interesting not only because it describes the dynamics of a tumbler filled with granular material which avalanches quickly, but also because it gives a physical example of a system in which complex behaviour is possible in the absence of the stretching and folding usually found in chaotic mixing devices. More precisely, the model system in the $\delta \to 0$ limit is an example of a *piecewise isometry*. These are discontinuous systems which can exhibit complicated fractal structures. The behaviour of piecewise isometries (PWIs) has been studied in some detail in recent years (e.g. Goetz 1998, 1999, 2000, 2001; Buzzi 2001; Ashwin & Fu 2002). Some applications of this type of

system have been described in Deane (2006), although most engineering applications to date have been concentrated on digital systems in signal processing.

The blinking flow for the three-dimensional spherical tumbler in the limit as $\delta \to 0$ can be viewed as a PWI on a curved surface. The dynamics of PWIs on a spherical surface were investigated in Scott, Holmes & Milburn (2001). The PWI can be understood by letting the time to cross the flowing layer tend to zero, while the depth of the flowing layer also tends to zero, or can be given explicitly by the following.

Consider a map H_P defined on the lower hemispherical shell (of radius l) $\mathscr{H}_l$ given by

$$\mathscr{H}_l = \{(x, y, z) | x^2 + y^2 + z^2 = l^2, z < 0\}.$$

We define the map by composing two rigid rotations. First, define a rigid rotation F_P about the x-axis, so that particle paths are constrained to sheets of constant x. Then, this rotation can be described by defining polar coordinates r and θ measured from $(x, 0, 0)$:

$$r^2 = y^2 + z^2,$$
$$\tan\theta = z/y,$$

where θ takes values in $[0, \pi]$ for negative z (i.e. it θ increases from 0 in the clockwise direction). Then, the map F_P is given by

$$F_P(x, r, \theta) = (x, r, \theta + A \pmod{\pi}),$$

where the (mod π) indicates that when a trajectory reaches the $z = 0$ plane at $(x', -y', 0)$ (leaving the lower hemisphere travelling upwards) it is 'reinjected' at $(x', y', 0)$ (that is, the circular surface forming the lid of the hemisphere is cut in two and the two halves identified along the line $y = 0, z = 0$). The dynamics of the map F_P can be described as a collection of periodic or quasi-periodic curves depending on whether A is rational or irrational.

Similarly define a map G_P by considering corresponding coordinates (y, ρ, ϕ), where ρ and ϕ are polar coordinates centred on $(0, y, 0)$ in Cartesian coordinates, given by

$$G_P(y, \rho, \phi) = (y, \rho, \phi + B \pmod{\pi}).$$

This is a similar rigid rotation about the y-axis, although the periodic identification of the lid of the hemisphere is different.

Finally, we compose these maps to form the piecewise isometry $H_P = G_P \circ F_P$. Formally, this can be written with the change of coordinates:

$$(y, \rho, \phi) = \mathscr{W}(x, r, \theta) = (r\cos\theta, \sqrt{x^2 + r^2\sin^2\theta}, \tan^{-1}(r\sin\theta)/x)$$

giving

$$H_P(x, r, \theta) = \mathscr{W}^{-1} \circ G_P \circ \mathscr{W} \circ F_P(x, r, \theta). \tag{3.7}$$

It is straightforward to see that the dynamics of H_P remain on a hemispherical shell, since it is composed of a pair of rotations about orthogonal axes.

An example of some of the rich dynamics in a PWI is shown in figure 17. In figure 17(a) we show a plan view of four trajectories with initial conditions on the hemisphere $x^2 + y^2 + z^2 = 0.49$ for the PWI H_P with $A = B = \pi/4$. This type of intricate fractal pattern is typical of PWIs, and similar dynamics can be seen in many of the cited references. Figures 17(b) to 17(d) show sample trajectories for the equivalent three-dimensional spherical mixer system, with $\omega_1 = \omega_2 = 0.5$ and $\tau_1 = \tau_2 = \pi/2$. To show the dynamics tending to the PWI dynamics, we choose $\dot{\gamma}_1 = \dot{\gamma}_2$ in these figures

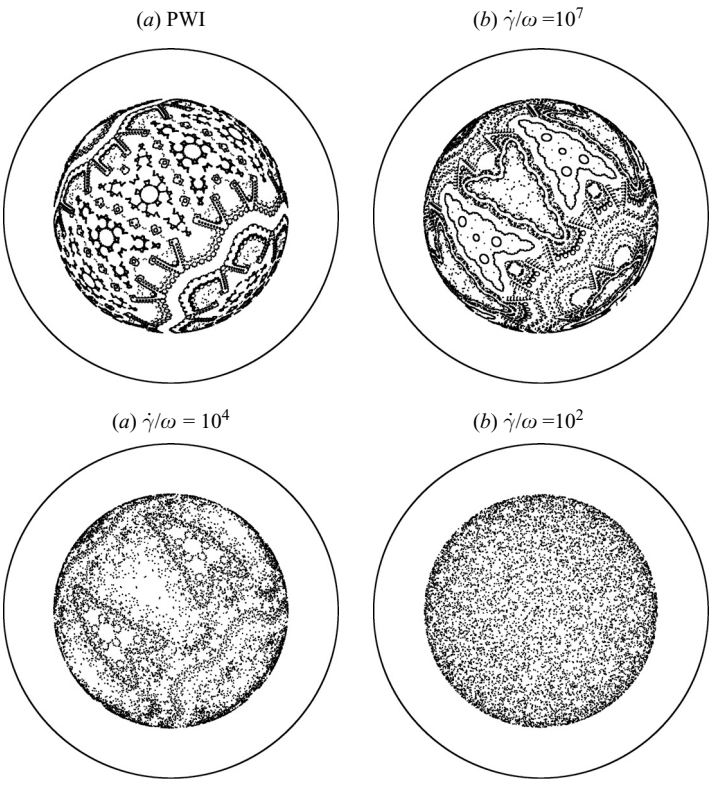

FIGURE 17. An example of how increasing the rate at which particles cross the flowing layer creates dynamics increasingly like that of a piecewise isometry. (*a*) The dynamics of a PWI with $A = B = \pi/4$ on the hemisphere $x^2 + y^2 + z^2 = 0.49$. (*b–d*) The corresponding map H_P with $\omega_1 = \omega_2 = 0.5$ and $\tau_1 = \tau_2 = \pi/2$ and varying values for $\dot{\gamma}$.

so that in figure 17(*b*), $\dot{\gamma}/\omega = 10^7$, in figure 17(*c*), $\dot{\gamma}/\omega = 10^4$ and in figure 17(*d*), $\dot{\gamma}/\omega = 10^2$.

This illustrates an interesting feature of the behaviour of the spherical tumbler. Complex behaviour in the three-dimensional system does not come solely from the shearing in different directions in the flowing layer associated with stretching and folding, but also from the rigid rotations on a curved surface. Note that a similar statement for the two-dimensional case does not hold – in the $\delta \to 0$ limit in this case, the dynamics simply reduces to quasi-periodic or periodic dynamics, depending whether the angle rotated through is irrational or rational.

3.7. *Mixing properties of three-dimensional rotating tumblers*

In § 2.4, we illustrated the mixing properties of a two-dimensional blinking tumbler. In this section, we contrast these results with the corresponding numerical experiment for the three-dimensional system. We again consider the evolution of two initial blobs (consisting of 16×10^4 points). Here, we begin by dividing a hemispherical shell into grey on the left and black on the right. Figures 18(*a*), 18(*f*) and 18(*k*) illustrate these initial conditions, viewing the hemisphere from below. Figures 18(*b*), 18(*c*), 18(*d*) and 18(*e*) show the images of the initial sets after 2, 4, 10 and 100 iterations respectively, of the piecewise isometry H_P (recall (3.7)), with angles $A = 3\pi/4$ and $B = 3\pi/4$. Note that mixing in this system is caused by a different mechanism from that in the

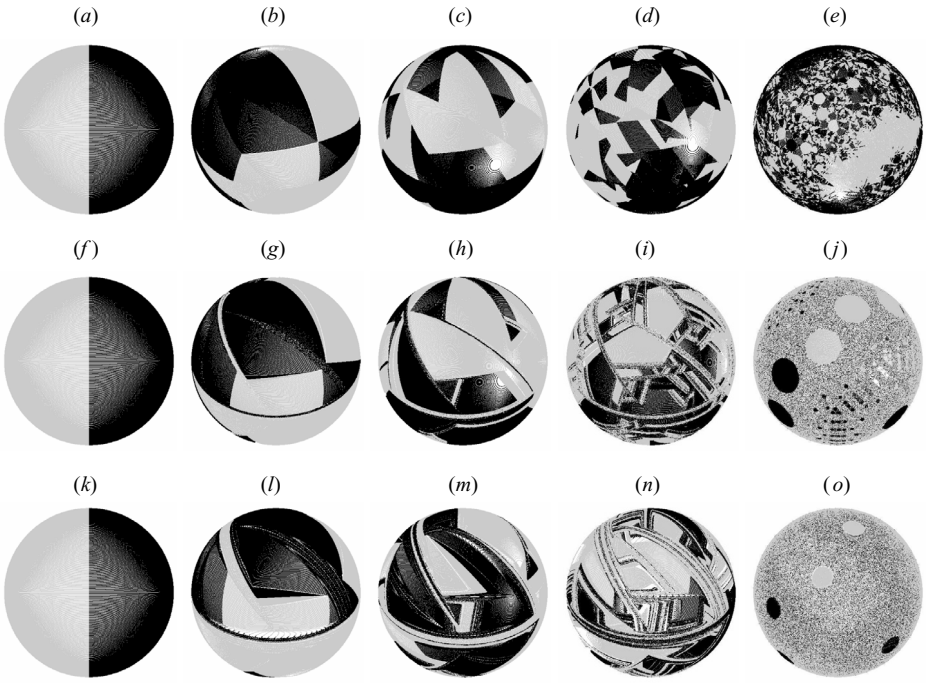

FIGURE 18. Comparison of the dynamical mixing properties of the piecewise isometry with the three-dimensional blinking tumbler. The images under the piecewise isometry H_P of the initial black and grey regions shown in (*a*) are shown after (*b*) 2, (*c*) 4, (*d*) 10 and (*e*) 100 iterations. The images in the middle and bottom rows are the same iteration of the same initial regions for the three-dimensional system $\mathcal{Q}$ with $\dot{\gamma}_{1,2} = 1000\omega_{1,2}$ (middle row) and $\dot{\gamma}_{1,2} = 100\omega_{1,2}$ (bottom row).

two-dimensional case. Here the discontinuities in the system cause the initial blobs to be cut and shuffled. There are no positive Lyapunov exponents and no stretching is involved. For small numbers of iterations it can be seen that mixing appears much more efficient than in the two-dimensional case (compare with figure 8). After 100 iterations the sets have become intricately intermingled, although some significant unmixed regions remain.

Figure 18(*g–j*) shows the images of the initial sets under the same numbers of iterations as the row above, for the three-dimensional system $\mathcal{Q}$ (recall (3.6)) for which the piecewise isometry is an idealization. That is, we take parameters $\tau_{1,2} = \pi/2$, $\omega_{1,2} = 3/2$ and $\dot{\gamma}_{1,2} = 1000\omega_{1,2}$. Figure 18(*l–o*) are again the same iterations, taking $\dot{\gamma}_{1,2} = 100\omega_{1,2}$. This final set of figures represent physically realizable parameters. For small numbers of iterations, it is clear that the three-dimensional system $\mathcal{Q}$ shares common features with the piecewise isometry. In particular, mixing begins to occur as a result of sets being divided across the flowing layer. After 10 iterations, two mixing mechanisms are apparent: cutting and shuffling due to PWI-like dynamics, and striated layers due to exponential stretching in the flowing-layer intersection. After 100 iterations, the exponential stretching dominates, and the mixed state displays a familiar chaotic sea punctuated by elliptic islands are periodic points. These figures are only a brief sample of the rich dynamical behaviour possible in this system, but they suggest that an understanding of the dynamics of the PWI will play a crucial role in the understanding of the three-dimensional blinking tumbler.

4. Outstanding problems, future directions and conclusions

The study of mixing of fluids benefited from the adoption of tools from nonlinear dynamics and its connection with chaos. The connection between the physical system, experiments, numerics and theory has now an established framework in which to study common issues across various problems. A natural question is whether or not a similar framework can be established in the field of granular mixing.

The work presented here aims to cover only part of this territory, that of mixing in systems undergoing motions driven by tumbling. We make the case for the application of recently developed theory to the study of a model flow of mixing of granular materials in rotated tumblers. Application to the two-dimensional case – a half-filled quasi-two-dimensional circular drum – can be analysed in terms of the existing mathematical formalism of linked twist maps. Conversely, the three-dimensional case – a half-filled sphere rotated among two orthogonal axes – does not benefit from an existing mathematical formalism. It is apparent that the mathematics of the three-dimensional case – a system we call a three-dimensional linked twist map – contains considerably more complexity, and opens an array of new questions. We initiate the study by showing some analytical results, two of them expressible as theorems. However, a number of open questions can immediately be proposed.

(i) Three-dimensional transport throughout the hemisphere. In the case of symmetric parameters we have shown that each trajectory remains on a particular hemispherical shell. To what extent is this true in the physical system? How should this be quantified? For non-symmetric parameters, the model allows a trajectory to leave its initial hemispherical shell. How efficient is transport in three dimensions in this case? Are there conditions in three dimensions where the mixing is 'ergodic and chaotic'?

(ii) Does a deeper understanding of the dynamics of piecewise isometries shed light on the kinematics of mixing for the three-dimensional spherical mixer?

(iii) We have described two different mechanisms for mixing in the three-dimensional spherical tumbler, one based on exponential stretching and folding characterized by positive Lyapunov exponents, the other on cutting and shuffling characterized by zero Lyapunov exponents. What is the relationship between the two mixing mechanisms? How can the mixing process be measured? What is the effect of each of these mechanisms on segregation?

There are also questions that clearly exceed the bounds of this paper. Here, we are taking it as an empirical fact that the segregated structures mimic the placement of islands in the system. We may imagine that, under the assumption that the flow affects segregation but segregation does not affect the flow, it is possible that such a state is an attractor in this dynamical system.

We recognize that the material presented here provides tools to 'solve' some problems, e.g. mixing in two-dimensional systems, but also opens a multitude of questions in the three-dimensional case, some of which may require the development of new mathematics.

We started these concluding remarks by asserting that the study of mixing of fluids had benefited from the adoption of tools from nonlinear dynamics and its connection with chaos. In the case of fluids, there has been, over the last two decades, a balance between experiments and theory. A perfect balance, however, is hard to achieve and we may argue that at various times, theory has been ahead of experiments and, at others, experiments have been ahead of the theory. The case of granular mixing and segregation in three-dimensional systems presents several immediate challenges and many of them lie on the experimental side – theory is ahead of experiments.

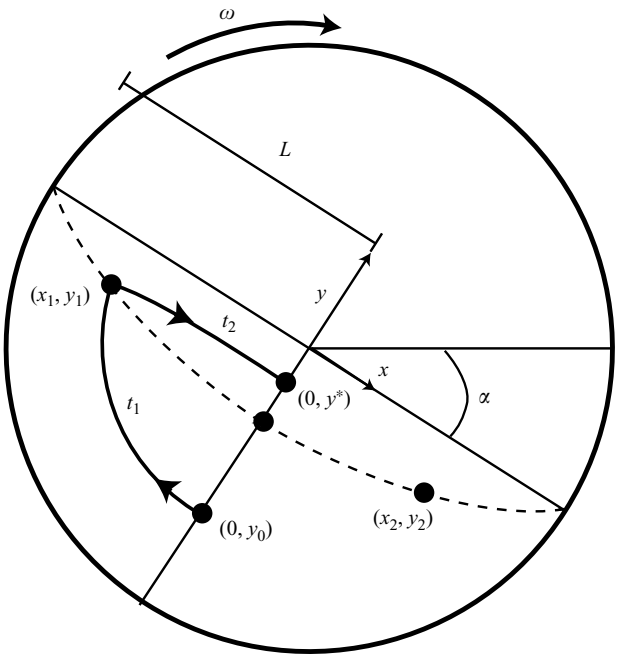

FIGURE 19. Geometry associated with the computation of the period of a point, i.e. the time required for a particle to make one complete revolution around the tumbler.

New experiments are required that are capable of studying systems undergoing non-symmetric motions on two axes. Two of the challenges are to design new devices, and to develop imaging techniques that allow for the visualization of the inner structure of the partially mixed structures.

The research of R. S. and S. W. was supported by ONR grant N00014-01-1-0769 and EPSRC grant EP/C515862/1. The support of S. W. M. and J. M. O. was supported in part by the Office of Basic Energy Sciences of the Department of Energy. S. W. M. also acknowledges support of an NSF graduate research fellowship. The authors thank Richard M. Lueptow for helpful conversations and Jan-Martin Hertzsch for preliminary numerical work.

Appendix A. Computation of the period in two dimensions, constant rotation rate

We compute the time taken for an arbitrary particle initially at $(0, y_0)$ in Cartesian coordinates to return to its original position. This calculation is most conveniently carried out by taking taking $(0, y_0)$ to be in the bulk, i.e. $y_0 \in (-\delta_0, -L)$. Figure 19 describes the geometry associated with the calculation.

At the intersection of bulk and flowing layer, (x_1, y_1), the particle lies on the intersection of the curves

$$y_0^2 = x_1^2 + y_1^2,$$
$$y_1 = -\delta(x_1) = -\sqrt{\omega/\dot{\gamma}}\sqrt{L^2 - x_1^2}.$$

The solution of these equations for a particle entering the flowing layer from the bulk (which means that we choose the negatively signed of the two solutions of each of

these equations) gives

$$x_1 = -\sqrt{\frac{L^2\omega - \dot{\gamma} y_0^2}{\omega - \dot{\gamma}}}, \tag{A 1}$$

$$y_1 = -\sqrt{\frac{\omega(y_0^2 - L^2)}{\omega - \dot{\gamma}}}. \tag{A 2}$$

Since in the bulk $\dot{x} = \omega y$, and the particle moves along the curve given by $x^2 + y^2 = y_0^2$, we can use these two expressions to derive an integral, which can be evaluated, for the time taken for the point $(0, y_0)$ to reach the boundary of the flowing layer:

$$\begin{aligned} t_1 &= \frac{1}{\omega}\int_0^{x_1} \frac{\mathrm{d}x}{\sqrt{y_0^2 - x^2}} \\ &= \left[\frac{1}{\omega}\tan^{-1}\left(\frac{x}{\sqrt{y_0^2 - x^2}}\right)\right]_0^{x_1}, \quad \text{where we substitute (A 1) for the upper limit,} \\ &= \frac{1}{\omega}\tan^{-1}\left(\sqrt{\frac{L^2\omega - \dot{\gamma} y_0^2}{\omega(y_0^2 - L^2)}}\right) \\ &= \frac{1}{\omega}\tan^{-1}\left(\frac{x_1}{y_1}\right). \end{aligned}$$

After the particle reaches (x_1, y_1) it continues along the streamline given by $\psi_f(x, y) = \text{const}$, with $\psi_f(x, y)$ given in (2.8), and where we have used the relation $\delta = \sqrt{\frac{\omega}{\dot{\gamma}}}\sqrt{L^2 - x^2}$. The constant is evaluated by requiring the level set of the stream-function to have the value that it assumes at (x_1, y_1):

$$\dot{\gamma}\left(\sqrt{\frac{\omega}{\dot{\gamma}}}\sqrt{L^2 - x^2} + \frac{y}{2}\right) y = \dot{\gamma}\left(\sqrt{\frac{\omega}{\dot{\gamma}}}\sqrt{L^2 - x_1^2} + \frac{y_1}{2}\right) y_1.$$

Substituting (A 1) for x_1 and (A 2) for y_1 into this expression leads to the further simplification:

$$\left(\sqrt{\frac{\omega}{\dot{\gamma}}}\sqrt{L^2 - x^2} + \frac{y}{2}\right) y = \frac{-\omega(y_0^2 - L^2)}{2(\omega - \dot{\gamma})}.$$

Next we solve this expression for y in terms of x, substitute the result into $\dot{x} = \dot{\gamma}(\delta(x) + y)$ to obtain a first-order ordinary differential equation in x. Integrating this equation from $x = x_1$ to $x = 0$, allows us to compute the time a particle requires to go from (x_1, y_1) to $(0, y^*)$, i.e. the time to cross half the flowing layer. After some algebra and integration, this is found to be given by the following simple expression:

$$t_2 = \frac{\pi}{2\sqrt{\omega\dot{\gamma}}}.$$

Therefore, $t_1 + t_2$ is the time required to complete half a circuit around the tumbler, and so by symmetry the period of the particle is

$$T = \frac{2}{\omega}\tan^{-1}\left(\sqrt{\frac{L^2\omega - \dot{\gamma} y_0^2}{\omega\left(y_0^2 - L^2\right)}}\right) + \frac{\pi}{\sqrt{\omega\dot{\gamma}}}.$$

It is a simple matter to use these formulae and calculations to obtain the angle variable defined in (2.10).

Appendix B. Proof of theorem 3.2

We will show that a particle always remains a constant distance r fom the origin whenever it is in the bulk. It should be clear that after entering the flowing layer, if the axis of rotation does not change during its passage through the flowing layer, then it exits the flowing layer and enters the bulk at the same radius from the origin. This follows from the fact that the particle remains on the same streamline so long as the axis of rotation is not changed. Therefore, we must show that if the axis of rotation is changed while the particle is in the flowing layer, then it exits the flowing layer at the same radial distance from the origin as when it entered the flowing layer.

We will prove our result in the case $\omega_1 = \omega_2 = \omega$ and $\dot{\gamma}_1 = \dot{\gamma}_2 = \dot{\gamma}$ for simplicity, although the same argument holds with only $\omega_1/\dot{\gamma}_1 = \omega_2/\dot{\gamma}_2$ (with considerably more algebra).

We begin by considering an initial point (x_0, y_0, z_0) satisfying $x_0^2 + y_0^2 + z_0^2 = r^2$, and let $x_0^2 + y_0^2 = r^2 - z_0^2 = \lambda^2$. Suppose, without loss of generality, that rotation is initially about the z-axis. Then $z = z_0$ is fixed and motion is along the curve given by $\psi_b = \omega(x^2 + y^2)/2 = \text{const}$. Hence, $\omega(x^2 + y^2)/2 = C_1 = \omega(x_0^2 + y_0^2)/2 = \omega\lambda^2/2$ and thus any (x, y, z_0) on this streamline in the bulk satisfies $x^2 + y^2 + z^2 = \lambda^2 + z_0^2 = r^2$. A similar argument holds for rotation about the x-axis.

Now suppose that rotation about the z-axis continues until the particle enters the flowing layer (otherwise, we would apply the same argument to rotation about the x-axis until the particle entered the flowing layer). At the intersection of the bulk and flowing layer, denoted by the point $(x_1, y_1, z_1 = z_0)$, the particle lies on the intersection of the curves

$$\lambda^2 = x_1^2 + y_1^2,$$
$$y_1 = -\delta_1(x_1, z_0),$$

where $\delta_1(x_1, z_0)$ is defined in (3.1). These equations can be solved for x_1 and y_1 (where we take the negatively signed solution of each equation which corresponds to the location of a particle entering the flowing layer) to give:

$$x_1 = -\sqrt{\frac{\lambda^2\dot{\gamma} - \omega\left(R^2 - z_0^2\right)}{\dot{\gamma} - \omega}},$$
$$y_1 = -\sqrt{\frac{\omega}{\dot{\gamma}}}\sqrt{\frac{-\dot{\gamma}\left(-R^2 + z_0^2 + \lambda^2\right)}{\dot{\gamma} - \omega}}.$$

These values are used to determine the constant which defines the streamline along which the particle will travel through the flowing layer, satisfying the streamfunction given by

$$\psi_f = \dot{\gamma}(\delta_1(x, z)y + y^2/2) = \text{const} = C_2 = \frac{-\dot{\gamma}\omega\left(R^2 - z_0^2 - \lambda^2\right)}{2(\dot{\gamma} - \omega)}.$$

Now suppose that rotation about the z-axis stops at an arbitrary point $(x_2, y_2, z_2 = z_0)$ within the flowing layer, and then we begin rotating about the x-axis. This fixes $x = x_2$, and motion now is along the streamline in the flowing layer given by

$$\psi_f = \dot{\gamma}(\delta_2(x, z)y + y^2/2) = \text{const} = C_3.$$

Note that by symmetry $C_2 = C_3$ as a consequence of our assumption that $\omega_1 = \omega_2 = \omega$ and $\dot{\gamma}_1 = \dot{\gamma}_2 = \dot{\gamma}$, but this is not necessarily the case if $\omega_1 \neq \omega_2$ and $\dot{\gamma}_1 \neq \dot{\gamma}_2$. Finally,

suppose that the particle follows this streamline under rotation about the x-axis until it reaches the boundary of the bulk and the flowing layer at the point $(x_3 = x_2, y_3, z_3)$, where y_3 and z_3 are the solutions of:

$$y_3 = -\delta_2(x_2, z_3),$$
$$C_3 = \dot{\gamma}\left(\delta(x_2, z_3)y_3 + y_3^2/2\right).$$

These equations can be solved to give:

$$y_3 = -\sqrt{-\frac{\omega\left(R^2 - z_0^2 - \lambda^2\right)}{\omega - \dot{\gamma}}}, \tag{B 1}$$

$$z_3 = \sqrt{R^2 - x_2^2 + \frac{\dot{\gamma}\left(R^2 - z_0^2 - \lambda^2\right)}{\omega - \dot{\gamma}}}. \tag{B 2}$$

Finally, we must verify that the particle exits the flowing layer at the same radial distance from the origin as when it first entered the flowing layer. This is accomplished by using (B 1) and (B 2) in the following calculation of the radial distance of the exiting particle from the origin:

$$\begin{aligned} x_3^2 + y_3^2 + z_3^2 &= x_2^2 - \frac{\omega\left(R^2 - z_0^2 - \lambda^2\right)}{\omega - \dot{\gamma}} + R^2 - x_2^2 + \frac{\dot{\gamma}\left(R^2 - z_0^2 - \lambda^2\right)}{\omega - \dot{\gamma}} \\ &= R^2 - \frac{(\omega - \dot{\gamma})\left(R^2 - z_0^2 - \lambda^2\right)}{(\omega - \dot{\gamma})} \\ &= \lambda^2 + z_0^2 \\ &= r^2. \end{aligned}$$

Appendix C. Computation of surface of period-one points for twist map corresponding to the rotation about one axis

We will derive conditions in terms of the parameters for which an integrable twist map, obtained from the steady velocity field corresponding to rotation with constant angular velocity about a single axis, has an 'ellipsoidal bowl' of period-one points in the bulk. Without loss of generality, we consider rotation about the z-axis.

A similar calculation to that in Appendix A for three dimensions gives the period of a point initially at $(0, y_0, z)$ under rotation about the z-axis to be

$$T(y_0, z) = \frac{2}{\omega_1}\tan^{-1}\left(\sqrt{\frac{\omega_1(R^2 - z^2) - \dot{\gamma}_1 y_0^2}{\omega_1\left(y_0^2 + z^2 - R^2\right)}}\right) + \frac{\pi}{\sqrt{\omega_1\dot{\gamma}_1}}, \tag{C 1}$$

since $L^2 = R^2 - z^2$. We assume that the map acts along trajectories for a time τ_1. Setting $T = \tau_1$ in (C 1), and inverting the result gives the necessary initial depth y_0 of a particle starting at $(0, y_0, z)$ to complete precisely one circuit around the tumbler in time τ_1:

$$y_0 = -\sqrt{\frac{\omega_1(R^2 - z^2)\left(1 + \tan^2\left[\frac{\omega_1}{2}\left(\tau_1 - \frac{\pi}{\sqrt{\omega_1\dot{\gamma}_1}}\right)\right]\right)}{\omega_1\tan^2\left[\frac{\omega_1}{2}\left(\tau_1 - \frac{\pi}{\sqrt{\omega_1\dot{\gamma}_1}}\right)\right] + \dot{\gamma}_1}}. \tag{C 2}$$

Now, for rotation about the z-axis, particle trajectories lie on the curves $x^2 + y^2 = \text{const} = y_0^2$. Substituting the expression for y_0 given in (C 2) into this equation gives

$$x^2 + y^2 + c_1 z^2 = c_2, \tag{C 3}$$

where, writing $\phi = \frac{\omega_1}{2}(\tau_1 - \frac{\pi}{\sqrt{\omega_1 \dot{\gamma}_1}})$,

$$c_1 = c_1(\omega_1, \dot{\gamma}_1, \tau_1) = \frac{\omega_1 \left(1 + \tan^2 \phi\right)}{\omega_1 \tan^2 \phi + \dot{\gamma}_1}, \tag{C 4}$$

$$c_2 = c_2(R, \omega_1, \dot{\gamma}_1, \tau_1) = \frac{R^2 \omega_1 \left(1 + \tan^2 \phi\right)}{\omega_1 \tan^2 \phi + \dot{\gamma}_1}. \tag{C 5}$$

Hence, we have shown that the period-one points of the twist map corresponding to a constant rotation rate about the z-axis lie on this ellipsoidal (actually part of a *prolate spheroid*) surface. Note that $c_2 = R^2 c_1$, and so, in the case of a unit sphere ($R = 1$), we have $c_1 = c_2$.

Appendix D. Intersection of prolate spheroids of period-one points

In Appendix 3, we showed that the period-one points of the twist map corresponding to rotation about the z-axis lie on an 'ellipsoidal bowl'. Similarly, by the same argument, it can be show that the twist map corresponding to rotation about the x-axis also lies on an 'ellipsoidal bowl'. In this section, we will describe the intersection of these two bowls.

In Appendix 3, we have shown that period-one points for rotation about the z-axis lie on the surface given by (C 3). Similarly, periodic points for rotation about the x-axis lie on the surface

$$c_3 x^2 + y^2 + z^2 = c_4,$$

where c_3 and c_4 have the corresponding expressions to (C 4) and (C 5), respectively. First, if $\tau_1 = \tau_2$, $\omega_1 = \omega_2$ and $\dot{\gamma}_1 = \dot{\gamma}_2$, then $c_1 = c_3 = \bar{c}$ and $c_2 = c_4 = \hat{c}$, and these surfaces intersect along the following sets:

$$\left.\begin{aligned} x^2 + y^2 + \bar{c} z^2 &= \hat{c} \\ \bar{c} x^2 + y^2 + z^2 &= \hat{c} \end{aligned}\right\} \Longrightarrow x^2 + \bar{c} z^2 = \bar{c} x^2 + z^2 \Longrightarrow x = \pm z,$$

(since $\bar{c} \neq 1$).

In the non-symmetric case, we have

$$x^2(1 - c_3) + z^2(c_1 - 1) = (c_2 - c_4),$$

which defines a pair of hyperbolas (as shown in figure 16). Suppose without loss of generality that $c_2 > c_4$ (e.g. $\tau_1 > \tau_2$ or $\omega_1 > \omega_2$); then the hyperbolas have semi-major axis $(c_2 - c_4)/(1 - c_3)$ and semi-minor axis $(c_2 - c_4)/(1 - c_1)$.

Appendix E. Stability of curves of periodic points (sketch of the hyperbolic points for the symmetric case)

Consider a point $(x, y, z) \in \Delta_{xz>0}$ and take a coordinate system (α, β, γ) where α lies in Σ_1, β lies in $\Delta_{xz>0}$, and γ lies in Σ_1. This is sketched in figure 20, which shows a section of the surfaces Σ_1 and Σ_2 for constant y, and the intersections Δ which should be imagined extending in the vertical direction. The point (x, y, z) is specified

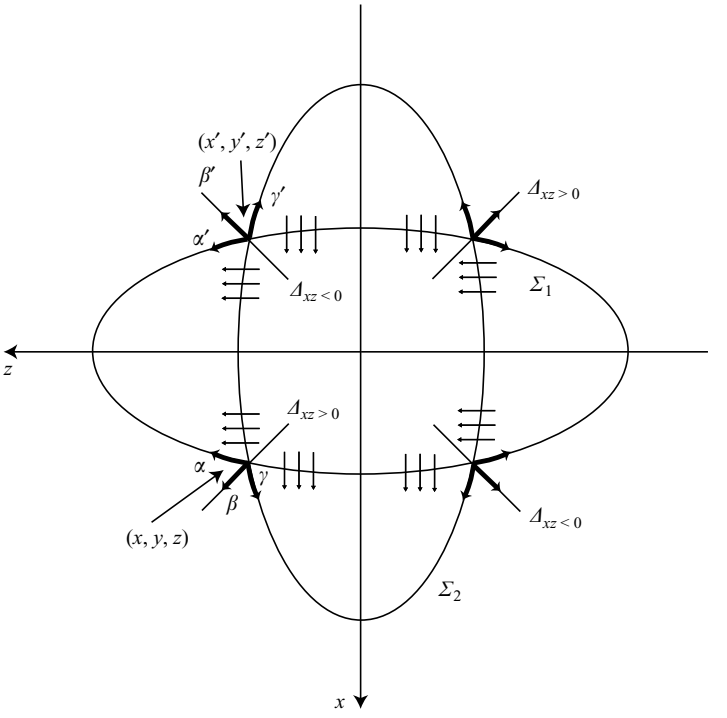

FIGURE 20. Illustration of coordinate systems and symmetries used in the stability of periodic points in Appendix E.

in the positive x and z quadrant, but the same argument applies in the opposite $\Delta_{xz>0}$ quadrant. The coordinate directions α, β, γ are shown as thick lines, and the direction of motion across the flowing layer is depicted by triple arrows.

Let J_1 be the Jacobian matrix for rotation for time τ_1 about the z-axis in this coordinate system. Since α and β lie within Σ_1, perturbations in these directions are fixed under rotation for time τ_1 about z. Thus, J_1 takes the form

$$J_1 = \begin{pmatrix} 1 & 0 & \epsilon_1 \\ 0 & 1 & \epsilon_2 \\ 0 & 0 & \epsilon_3 \end{pmatrix},$$

where ϵ_1, ϵ_2, ϵ_3 are three constants whose sign could be deduced from careful consideration of the dynamics. Now consider the same point under rotation about the x-axis using the same coordinate system. Here, perturbations in the β and γ directions are fixed, and, by symmetry, the Jacobian matrix J_2 for rotation about the x-axis takes the form

$$J_2 = \begin{pmatrix} \epsilon_3 & 0 & 0 \\ \epsilon_2 & 1 & 0 \\ \epsilon_1 & 0 & 1 \end{pmatrix}.$$

Stability of such a point (x, y, z) is then given by the eigenvalues of $(MJ_2M^{-1})(MJ_1M^{-1}) = MJ_2J_1M^{-1}$, where M is the appropriate change of coordinate matrix (since (α, β, γ) do not form an orthonormal set of directions). Note that since $\det(MJ_2J_1M^{-1}) = \det(J_2J_1)$ and $\mathrm{tr}(MJ_2J_1M^{-1}) = \mathrm{tr}(J_2J_1)$ (by cyclic permutation of

the matrices), it is sufficient to inspect the eigenvalues of

$$J_2 J_1 = \begin{pmatrix} \epsilon_3 & 0 & \epsilon_1\epsilon_3 \\ \epsilon_2 & 1 & \epsilon_2(1+\epsilon_3) \\ \epsilon_1 & 0 & \epsilon_1^2+\epsilon_3 \end{pmatrix}.$$

Clearly one eigenvalue is 1. Computing the determinate $\det(J_2 J_1) = \epsilon_3^2$ implies that $\epsilon_3 = \pm 1$, since the map is area-preserving, which leaves the other pair of eigenvalues $\lambda_{+,-} = (2 + \epsilon_1^2 \pm \sqrt{\epsilon_1^2(\epsilon_1^2+4)})/2$. Hence, we have $\lambda_+ > 1$, $\lambda_- < 1$ and (x, y, z) is hyperbolic.

REFERENCES

Aharonov, D. & Elias, U. 1990 Parabolic fixed points, invariant curves, and action-angle variables. *Ergod. Theory Dyn. Sys.* **10**, 231–245.

Aref, H. 1984 Stirring by chaotic advection. *J. Fluid Mech.* **143**, 1–21.

Ashwin, P. & Fu, X. C. 2002 On the geometry of orientation-preserving planar piecewise isometries. *J. Nonlinear Sci.* **12**, 207–240.

Bridgwater, J., Sharpe, N. W. & Stocker, D. C. 1969 Particle mixing by percolation. *Trans. Inst. Chem. Engng* **47**, T114–T119.

Brucks, A., Arndt, T., Ottino, J. M. & Lueptow, R. M. 2007 Behavior of flowing granular materials under variable *g*. *Phys. Rev.* E **75**, 032301.

Burton, R. & Easton, R. 1980 Ergodicity of linked twist mappings. In *Proc. Intl Conf. Northwestern Univ., Evanston, Ill, 1979*. Lecture Notes in Mathematics, vol. 819, pp. 35–49. Springer.

Buzzi, J. 2001 Piecewise isometries have zero topological entropy. *Ergod. Theory Dyn. Sys.* **21**, 1371–1377.

Cantelaube, F. & Bideau, D. 1995 Radial segregation in a 2d drum: an experimental analysis. *Europhys. Lett.* **30**, 133–138.

Cisar, S. E., Umbanhowar, P. B. & Ottino, J. M. 2006 Radial granular segregation under chaotic flow in two-dimensional tumblers. *Phys. Rev.* E **74**, 051305.

Clément, E., Rajchenbach, J. & Duran, J. 1995 Mixing of a granular material in a bidimensional rotating drum. *Europhys. Lett.* **30**, 7–12.

Dasgupta, S., Khakhar, D. V. & Bhatia, S. K. 1991 Axial transport of granular solids in horizontal rotating cylinders. 1. Theory. *Powder Technol.* **67**, 145–151.

Deane, J. H. B. 2006 Piecewise isometries: applications in engineering. *Meccanica* **41**, 241–252.

Devaney, R. L. 1978 Subshifts of finite type in linked twist mappings. *Proc. Am. Math. Soc.* **71**, 334–338.

Devaney, R. L. 1980 Linked twist mappings are almost Anosov. In *Proc. Intl Conf. Northwestern Univ., Evanston, Ill. 1979*. Lecture Notes in Mathematics, vol. 819, pp. 121–145. Springer.

Donald, M. B. & Roseman, B. 1962 Mixing and demixing of solid particles. Part 1. Mechanisms in a horizontal drum mixer. *Brit. Chem. Engng* **7**, 749–753.

Duran, J. 2000 *Sands, Powders, and Grains: An Introduction to the Physics of Granular Materials*. Springer.

Dury, C. M. & Ristow, G. H. 1997 Radial segregation in a two-dimensional rotating drum. *J. Phys.* I **7**, 737–745.

Elperin, T. & Vikhansky, A. 2000 Granular flow in a three-dimensional rotating container. *Phys. Rev.* E **62**, 4446–4449.

Elperin, T. & Vikhansky, A. 2002 Variational model of granular flow in a three-dimensional rotating container. *Physica* A **303**, 48–56.

Fiedor, S. J. & Ottino, J. M. 2003 Dynamics of axial segregation and coarsening of dry granular materials and slurries in circular and square tubes. *Phys. Rev. Lett.* **91**, 244301.

Fiedor, S. J. & Ottino, J. M. 2005 Mixing and segregation of granular matter: multi-lobe formation in time-periodic flows. *J. Fluid Mech.* **533**, 223–236.

Fiedor, S. J., Umbanhowar, P. & Ottino, J. M. 2006 Dynamics of axial segregation in granular slurries: parallel experiments and influence of aspect ratio and periodic tilting. *Phys. Rev.* E **73**, 041303.

Fountain, G. O., Khakhar, D. V. & Ottino, J. M. 1998 Visualization of three-dimensional chaos. *Science* **281**, 683–686.

Fukushima, E. 1999 Nuclear magnetic resonance as a tool to study flow. *Annu. Rev. Fluid Mech.* **31**, 95–123.

Gilchrist, J. F. & Ottino, J. M. 2003 Competition between chaos and order: mixing and segregation in a spherical tumbler. *Phys. Rev.* E **68**, 061303.

Goetz, A. 1998 Dynamics of a piecewise rotation. *Continuous and Discrete Dynamical Systems* **4**, 593–608.

Goetz, A. 1999 Sofic subshifts and piecewise isometric systems. *Ergod. Theory Dyn. Sys.* **19**, 1485–1501.

Goetz, A. 2000 Dynamics of piecewise isometries. *Illinois J. Maths* **44**, 465–478.

Goetz, A. 2001 Piecewise isometries – an emerging area of dynamical systems. In *Trends Math: Fractals in Graz 2001*, pp. 135–144.

Henein, H., Brimacombe, J. K. & Watkinson, A. P. 1983 Experimental-study of transverse bed motion in rotary kilns. *Metall. Trans.* B **14**, 191–205.

Hill, K. M., Caprihan, A. & Kakalios, J. 1997 Bulk segregation in rotated granular material measured by magnetic resonance imaging. *Phys. Rev. Lett.* **78**, 50–53.

Hill, K. M., Khakhar, D. V., Gilchrist, J. F., McCarthy, J. J. & Ottino, J. M. 1999 Segregation-driven organization in chaotic granular flows. *Proc. Natl Acad. Sci.* **96**, 11701–11706.

Jain, N., Ottino, J. M. & Lueptow, R. M. 2002 An experimental study of the flowing granular layer in a rotating tumbler. *Phys. Fluids* **14**, 572–582.

Jain, N., Ottino, J. M. & Lueptow, R. L. 2005*a* Combined size and density segregation and mixing in noncircular tumblers. *Phys. Rev.* E **71**, 051301–1–051031–10.

Jain, N., Ottino, J. M. & Lueptow, R. M. 2005*b* Regimes of segregation and mixing in combined size and density granular systems: an experimental study. *Granul. Matter* **7** (2–3), 69–81.

Khakhar, D. V., McCarthy, J. J., Shinbrot, T. & Ottino, J. M. 1997 Transverse flow and mixing of granular materials in a rotating cylinder. *Phys. Fluids* **9** (1), 31–43.

Khakhar, D. V., McCarthy, J. J., Gilchrist, J. F. & Ottino, J. M. 1999 Chaotic mixing of granular materials in two-dimensional tumbling mixers. *Chaos* **9**, 195–205.

Khakhar, D. V., Orpe, V. O. & Ottino, J. M. 2001 Surface granular flows: two related examples. *Adv. Complex Sys.* **4**, 407–417.

Khan, Z. S. & Morris, S. W. 2005 Subdiffusive axial transport of granular materials in a long drum mixer. *Phys. Rev. Lett.* **94**, 048002.

Khan, Z. S., Tokaruk, W. A. & Morris, S. W. 2004 Oscillatory granular segregation in a long drum mixer. *Europhys. Lett.* **66**, 212–218.

Makse, H. A. 1999 Continuous avalanche segregration of granular mixtures in thin rotating tumblers. *Phys. Rev. Lett.* **83**, 3186–3189.

Meier, S. W., Cisar, S. E., Lueptow, R. M. & Ottino, J. M. 2006 Capturing patterns and symmetries in chaotic granular flow. *Phys. Rev.* E **74**, 031310.

Meier, S. W., Lueptow, R. M. & Ottino, J. M. 2007 A dynamical systems approach to mixing and segregation of granular materials in tumblers. *Adv. Phys.* **56**, 757–827.

Mellmann, J. 2001 The transverse motion of solids in rotating cylinders – forms of motion and transition behavior. *Powder Technol.* **118**, 251–270.

Metcalfe, G. & Shattuck, M. 1996 Pattern formation during mixing and segregation of flowing granular materials. *Physica* A **233**, 709–717.

Mezic, I. 2001 Break-up of invariant surfaces in action-angle-angle maps and flows. *Physica* D **154**, 51–67.

Mezic, I. & Wiggins, S. 1994 On the integrability and perturbation of three-dimensional fluid flows with symmetry. *J. Nonlinear Sci.* **4**, 157–194.

Nakagawa, M., Altobelli, S. A., Caprihan, A., Fukushima, E. & Jeong, E. K. 1993 Noninvasive measurements of granular flows by magnetic resonance imaging. *Exps. Fluids* **16**, 54–60.

Ottino, J. M. 1989 *The Kinematics of Mixing: Stretching, Chaos, and Transport*. Cambridge University Press.

Ottino, J. M. & Khakhar, D. V. 2000 Mixing and segregation of granular materials. *Annu. Rev. Fluid Mech.* **32**, 55–91.

Pohlman, N. A., Meier, S. W., Lueptow, R. M. & Ottino, J. M. 2006*a* Surface velocity in three-dimensional granular tumblers. *J. Fluid Mech.* **560**, 355–368.

Pohlman, N. A., Ottino, J. M. & Lueptow, R. M. 2006*b* End wall effects in granular tumblers: from quasi-2d flow to three-dimensional flow. *Phys. Rev.* E **74**, 031305.

Przytycki, F. 1983 Ergodicity of toral linked twist mappings. *Ann. Sci. Ecole Norm. Sup.* **16**, 345–354.

Rajchenbach, J. 1990 Flow in powders: from discrete avalanches to continuous regime. *Phys. Rev. Lett.* **65**, 2221–2224.

Ristow, G. H. 1994 Particle mass segregation in a 2-dimensional rotating drum. *Europhys. Lett.* **28**, 97–101.

Ristow, G. H. 2000 *Pattern Formation in Granular Materials*. Springer Tracts in Modern Physics, vol. 164. Springer.

Samelson, R. M. & Wiggins, S. 2006 *Lagrangian Transport in Geophysical Jets and Waves: The Dynamical Systems Approach*. Springer.

Scott, A. J., Holmes, C. A. & Milburn, G. J. 2001 Hamiltonian mappings and circle packing phase spaces. *Physica* D **155**, 34–50.

Simo, C. 1980 Invariant curves near parabolic points and regions of stability. In *Proc. Intl Conf. Northwestern Univ., Evanston, Ill, 1979* Lecture Notes in Mathematics, vol. 819, pp. 418–424. Springer.

Simo, C. 1982 Stability of degenerate fixed points of analytic area preserving maps. *Asterisque* **98–99**, 184–194.

Sturman, R., Ottino, J. M. & Wiggins, S. 2006 *The Mathematical Foundations of Mixing*. Cambridge Monographs on Applied and Computational Mathematics, vol. 22. Cambridge University Press.

Wiggins, S. 1994 *Normally Hyperbolic Invariant Manifolds in Dynamical Systems*. Springer.

Wiggins, S. 2003 *Introduction to Applied Nonlinear Dynamical Systems and Chaos*, 2nd edn. Springer.

Wiggins, S. & Holmes, P. J. 1987 Periodic orbits in slowly varying oscillators. *SIAM J. Math. Anal.* **18**, 592–611.

Wightman, C. & Muzzio, F. J. 1998*a* Mixing of granular material in a drum mixer undergoing rotational and rocking motions – I. Uniform particles. *Powder Technol.* **98**, 113–124.

Wightman, C. & Muzzio, F. J. 1998*b* Mixing of granular material in a drum mixer undergoing rotational and rocking motions – II. Segregating particles. *Powder Technol.* **98**, 125–134.

Wightman, C., Mort, P. R., Muzzio, F. J., Riman, R. E. & Gleason, E. K. 1995 The structure of mixtures of particles generated by time-dependent flows. *Powder Technol.* **84**, 231–240.

Wightman, C., Moakher, M., Muzzio, F. J. & Walton, O. 1998 Simulation of flow and mixing of particles in a rotating and rocking cylinder. *AIChE J.* **44**, 1266–1276.

Wojtkowski, M. 1980 Linked twist mappings have the K-property. In *Nonlinear Dynamics (Intl Conf., New York, 1979)*, *Ann. New York Acad. Sci.*, vol. 357, pp. 65–76.